

A SUPERFAST DIRECT INVERSION METHOD FOR THE NONUNIFORM DISCRETE FOURIER TRANSFORM *

HEATHER WILBER[†], ETHAN N. EPPERLY[‡], AND ALEX H. BARNETT[§]

Abstract. A direct solver is introduced for solving overdetermined linear systems involving nonuniform discrete Fourier transform matrices. Such a matrices can be transformed into a Cauchy-like form that has hierarchical low rank structure. The rank structure of this matrix is explained, and it is shown that the ranks of the relevant submatrices grow only logarithmically with the number of columns of the matrix. A fast rank-structured hierarchical approximation method based on this analysis is developed, along with a hierarchical least-squares solver for these and related systems. This result is a direct method for inverting nonuniform discrete transforms with a complexity that is nearly linear with respect to the degrees of freedom in the problem. This solver is benchmarked against various iterative and direct solvers in the setting of inverting the one-dimensional type-II (or forward) transform, for a range of condition numbers and problem sizes (up to 4×10^6 by 2×10^6). These experiments demonstrate that this method is especially useful for large ill-conditioned problems with multiple right-hand sides.

Key words. nonuniform discrete Fourier transform, Vandermonde, rank structured least-squares, displacement structure, hierarchical matrices, rectangular linear systems

AMS subject classifications. 65T50, 65F55, 65F20

1. Introduction. The nonuniform discrete Fourier transform (NUDFT) is a fundamental task in computational mathematics. In one dimension, the forward problem is to evaluate

$$b_j = \sum_{k=1}^n e^{-2\pi i p_j w_k} x_k, \quad 1 \leq j \leq m, \quad (1.1)$$

where the *sample locations* $0 \leq p_m < \dots < p_1 < 1$, the *frequencies* $0 \leq w_1 < \dots < w_n < n$, and the *coefficients* $\{x_1, \dots, x_n\}$ are provided. In this paper we will focus on the so-called *type-II transform* [20] for which the frequencies $w_k = k - 1$ are equispaced. The forward problem (1.1) then corresponds to evaluating a given 1-periodic Fourier series at real targets $\{p_j\}_{j=1}^m$, which naively involves $\mathcal{O}(mn)$ operations. There exist well-established algorithms based upon the fast Fourier transform (FFT) [5, 20, 26, 39, 49, 51] that compute the type-II transform approximately at a reduced complexity $\mathcal{O}(n \log n + m \log(1/\epsilon))$, where ϵ is an accuracy parameter. Mature software implementations of these fast transforms are available such as NFFT¹ [33] and FINUFFT² [5]. In this article, we focus on the *inverse* problem:

Inverse type-II NUDFT problem. Given measurements $b = (b_1, \dots, b_m)^T \in \mathbb{C}^m$ and locations $\{p_j\}_{j=1}^m$, determine the coefficients $x = (x_1, \dots, x_n)^T \in \mathbb{C}^n$.

Unlike for the plain discrete Fourier transform (DFT), inversion of the type-II is not simply an application of its adjoint (type-I) transform; rather, a large dense $m \times n$ linear system

*Funding: This work is partly supported by the National Science Foundation grant DMS-2103317 and FRG award 1952777, the Carver Mead New Horizons Fund, and the U.S. Department of Energy, Office of Science, Office of Advanced Scientific Computing Research, Department of Energy Computational Science Graduate Fellowship under award number DE-SC0021110.

[†]Department of Applied Mathematics, University of Washington, Seattle, WA, 98105, United States (hdw27@uw.edu).

[‡]Division of Computing and Mathematical Sciences, California Institute of Technology, Pasadena, CA, 91125, United States (eepperly@caltech.edu).

[§]Center for Computational Mathematics, Flatiron Institute, New York, NY, 10010, United States (abarnett@flatironinstitute.org).

¹Available at <https://github.com/NFFT/nfft>

²Available at <https://finufft.readthedocs.io>

must be solved. This task, and its higher-dimensional generalizations, is important in diverse applications including geophysics [53, 67], astrophysics [55], signal and image processing [4, 22, 59], and other areas of computational mathematics [42, 47]. In particular, type-II inverse NUDFT solvers can be used to reconstruct an image from irregularly sampled Fourier data, as occurs in non-Cartesian magnetic resonance imaging (MRI) [23, 27, 35, 46] and synthetic aperture radar (SAR) [25].

In this article, we develop a new direct solver for the type-II inverse NUDFT problem with complexity $\mathcal{O}((m+n)\log^2 n \log^2(1/\epsilon))$. Our strategies are related to ideas that have been proposed for solving Toeplitz linear systems [62, 64], but they appear to be new in this context. The method we develop leverages displacement structure [32, 36], low rank approximation, and hierarchical numerical linear algebra [8, 28]. It is markedly different from other methods for the inverse NUDFT problem such as iterative solvers [22, 23, 27, 51] and recent direct methods combining sparse weights with the adjoint transform [34, 35]. Our solver is general-purpose and fully adaptive, requiring no tuning parameters from the user other than a prescribed error tolerance. Unlike all of the above-mentioned methods, our approach is highly robust to sampling locations and can be applied in problems where sample locations are clustered or irregular. It is also particularly fast for problems that involve multiple right-hand sides.

1.1. Problem formulation. This paper focuses primarily on the inverse type-II NUDFT problem in the one-dimensional setting (1.1), where the system is overdetermined (i.e., the number of measurements m equals or exceeds the number of unknowns n). The extension to type-I NUDFT inversion is straightforward, and we briefly discuss other extensions in section 6. Define the NUDFT matrix $V \in \mathbb{C}^{m \times n}$ to have entries

$$V_{jk} = \gamma_j^{k-1}, \quad \text{where } \gamma_j = e^{-2\pi i p_j}, \quad \text{for } j = 1, \dots, m, k = 1, \dots, n.$$

The matrix V is a *Vandermonde matrix*, and $\gamma_1, \dots, \gamma_m$ are referred to as the *nodes* of V . We assume the sample locations are distinct and ordered so that $0 \leq p_m < \dots < p_1 < 1$. This ensures that the nodes are unique and arranged counterclockwise around the unit circle. One can permute the rows of V to order the sample locations in this way. The inverse type-II NUDFT problem consists of solving $Vx = b$ in the least-squares sense:

$$x = \operatorname{argmin}_{x \in \mathbb{C}^n} \|Vx - b\|_2^2. \quad (1.2)$$

We include the noisy-data case where b is not in the range of V , important in applications where correct averaging over an excess of data reduces the noise in the solution x . Since γ_j are distinct, V has full rank. While we allow that V may be ill-conditioned, we assume that V is numerically full-rank, in sense that the condition number

$$\kappa_2(V) = \frac{\sigma_{\max}(V)}{\sigma_{\min}(V)} \quad (1.3)$$

is much smaller than the inverse machine precision. Here, $\sigma_{\max}(V)$ and $\sigma_{\min}(V)$ denote the largest and smallest singular values of V . For ease of notation, we make the simplifying assumption that n is a power of two. We emphasize that our algorithm works for any n , not just powers of two.

REMARK 1. *There are many conventions in the literature for the type-II (forward) transform, varying in the sign of the exponential, presence or absence of the 2π factor, and whether frequency indices are symmetric about zero (compare, e.g., [5, 20, 33, 34, 56]). Ours is close to that for the plain DFT. Conversions between conventions can be performed numerically using simple linear-time operations on inputs or outputs.*

1.2. From Vandermonde to Cauchy-like. The fundamental idea behind our direct inversion method is to transform from a problem involving a Vandermonde matrix to an equivalent problem involving a Cauchy-like matrix $C = VF^*$, where F is a DFT matrix defined below in (1.5). This transformation is useful because C has low rank properties that can be analyzed and exploited. Similar ideas have been proposed for fast direct Toeplitz solvers [60, 61, 64], though key details turn out to be quite different in this setting.

We begin by observing that V satisfies the Sylvester matrix equation

$$\Gamma V - VQ = uv^*, \quad (1.4)$$

where $(\cdot)^*$ denotes the Hermitian transpose, uv^* is a rank 1 matrix, $Q = \begin{pmatrix} 0 & 1 \\ 1 & 0 \end{pmatrix} \in \mathbb{C}^{n \times n}$ is the circular shift-down matrix, and

$$\Gamma = \text{diag}(\gamma_1, \dots, \gamma_m).$$

Specifically, u has j th entry $\gamma_j^n - 1$, while $v^* = [0, \dots, 0, 1]$. Let F be the normalized DFT matrix

$$F_{jk} = \omega^{j(2k-1)} / \sqrt{n} \quad \text{for } 1 \leq j, k \leq n \quad \text{where } \omega = e^{\pi i/n}. \quad (1.5)$$

The circulant matrix Q is diagonalized by F :

$$FQF^* = \Lambda := \text{diag}(\omega^2, \omega^4, \dots, \omega^{2n}).$$

Letting $C = VF^*$, it follows from (1.4) and $FF^* = I$ that

$$\Gamma C - C\Lambda = ww^*, \quad (1.6)$$

where we have defined $w = Fv$, and this in turn implies that

$$C_{jk} = \frac{u_j \overline{w_k}}{\Gamma_{jj} - \Lambda_{kk}} = \frac{u_j \overline{w_k}}{\gamma_j - \omega^{2k}}. \quad (1.7)$$

A matrix with the structure $C_{jk} = a_j b_k / (c_j - d_k)$ for numbers $\{a_j\}$, $\{b_k\}$, $\{c_j\}$, and $\{d_k\}$ is called a *Cauchy-like matrix* [36]. The algebraic structure of these matrices is useful in various ways [32]. For example, one can generate subblocks of C using (1.7) (or related formulas), which only require accessing entries in four vectors. In addition to its algebraic structure, C possesses many submatrices that have low numerical rank. As we detail precisely in section 3, the low rank structure of C depends on the distribution of the nodes $\{\gamma_1, \dots, \gamma_m\}$ relative to the n th roots of unity $\{\omega^2, \omega^4, \dots, \omega^{2n}\}$. Our analysis of the rank structure of C is constructive and uses the displacement relation (1.6). We show that one can cheaply generate low rank approximations for these submatrices using small Sylvester matrix equations related to (1.6). This allows us to construct an hierarchical approximation to C while never explicitly forming or storing C and its relevant submatrices.

1.3. A displacement-based superfast solver. Our proposed direct solver approximates a least-squares solution to $Cy = b$, and then returns $x = F^*y$. The latter is an approximate solution to (1.2), recalling that $C = VF^*$. The solver is described in pseudocode in Algorithm 1.1. It employs the following ingredients, which we develop over the course of the rest of the paper:

- **Hierarchical rank structure.** In section 2, we show that C can be approximated to high accuracy by a matrix H which possesses hierarchical low rank structure under the hierarchical semiseparable (HSS) format [15, 16, 43]. For an approximation tolerance ϵ , the off-diagonal blocks of H have rank at most k , where

$$k \leq \left\lceil \frac{2 \log(4/\epsilon) \log(4n)}{\pi^2} \right\rceil = \mathcal{O}(\log(n) \log(1/\epsilon)). \quad (1.8)$$

Algorithm 1.1 A superfast least-squares solver for $Vx = b$. (Type-II NUDFT inversion)

- 1: Compute $w = Fv$, where v is as in (1.4).
 - 2: Use ADI and (1.6) to generate $H \approx C$, where H is a rectangular HSS matrix (see section 3)
 - 3: Solve $Hy = b$ in the least-squares sense (see section 4).
 - 4: Compute $x = F^*y$.
-

- **Superfast construction by ADI.** We provide a construction algorithm for $H \approx C$ that combines the factored alternating direction implicit (ADI) method [10, 57] with an interpolative decomposition [17]. This algorithm runs in complexity $\mathcal{O}(mk^2) = \mathcal{O}(m \log^2(n) \log^2(1/\epsilon))$ time.
- **Superfast least-squares solver.** For a square HSS matrix H with off-diagonal blocks of rank k , the linear system $Hx = b$ can be solved in $\mathcal{O}(mk^2)$ operations [15, 43]. Less work has focused on the least-squares case. A semidirect method based on recursive skeletonization is described in [29]. The $\mathcal{O}(mk^2)$ solver we develop here is a generalization of the specialized least-squares solver for overdetermined Toeplitz systems introduced in [62].

While our compression strategy takes special advantage of the displacement structure of C , our least-squares solver (step 4 in Algorithm 1.1) is generic and can be applied to any rectangular system with HSS rank structure.

1.4. Related work. There are many approaches to the inverse NUDFT problem, and we can only give a brief overview (also see [35, Sec. 1]). Standard approaches include (i) working directly with the system $Vx = b$, (ii) working with the normal equations, $V^*Vx = V^*b$, and (iii) working with the the adjoint (or “second kind”) normal equations, $VV^*y = b$. Variants which sandwich a diagonal weight matrix between V and V^* also exist [22, 35].

A major class of methods for solving these systems is the iterative methods, which can leverage fast implementations of the forward NUDFT transform. Since the normal and adjoint normal linear systems are positive semidefinite, the conjugate gradient (CG) method can be applied [22, 23, 51, 52]. This is especially appealing for the normal equations since V^*V is a Toeplitz matrix, for which a fast matrix-vector product is available via a pair of padded FFTs (whose prefactor is smaller than that of NUDFT transforms). The adjoint normal matrix VV^* is not in general Toeplitz, but may still be applied via a pair of NUDFTs (a type-I followed by a type-II). Iterative methods are quite effective as long as V is well-conditioned. However, convergence rates for these methods depend on the condition number $\kappa_2(V)$, defined in (1.3). Unless strong restrictions are placed on the sample locations [19, 22, 51, 65], $\kappa_2(V)$ can increase without bound. Diagonal preconditioners for the above normal systems have been developed, based on local sampling spacings (Voronoi weights) [22], or weights which optimize the Frobenius-norm difference from the pseudoinverse (so-called “sinc² weights”) [27]. These are related to density compensation (or “gridding”) weights in MRI [46]. Moving beyond diagonal preconditioners, Toeplitz systems also have various circulant preconditioners available that exploit the FFT [14].

Another class of methods are the direct methods. These have some advantages over iterative methods in some settings:

- **Poor conditioning.** In many applications, the sample locations may be highly irregular, clustered, or have regions of low density relative to the shortest Fourier wavelength.

For these problems, V is ill-conditioned, and iterative methods may converge slowly or not at all [22]. In contrast, the runtime of a direct solver does not depend on

problem conditioning.

- **Multiple right-hand sides.** Some applications involve solving a sequence of inverse NUDFT problems with the same sample locations $\{p_j\}_{j=1}^m$ but many different right-hand sides b . For direct solvers which factor the matrix V (or the transformed matrix C), the factorization can be stored and reused to solve multiple right-hand sides quickly (e.g. for our solver, $\mathcal{O}(mk)$ operations per right-hand side for the numerical rank k considered in (1.8)).

The $\mathcal{O}(mn^2)$ cost of dense, unstructured direct methods (e.g., column-pivoted QR) makes them essentially useless beyond a few tens of thousands of unknowns. Turning to fast direct methods, one class is based on the normal

equations, which can be solved by fast [24, 32] or superfast direct Toeplitz solvers [60, 64]. However, for ill-conditioned problems, normal equations-based direct solvers can have substantially reduced accuracy as the condition number for the normal equations is equal to the square of the original matrix, $\kappa_2(V^*V) = \kappa_2(V)^2$. Our direct solver works directly with V to avoid this issue.

Another direct method was developed in [34], which we refer to as the Kircheis–Potts algorithm. This method is based on an optimization routine that finds a specially structured matrix Ψ such that $V\Psi \approx mI$. Constructing Ψ requires $\mathcal{O}(m^2 + n^2)$ operations, which can be prohibitive in large-scale settings. However, once constructed, Ψ can be applied to right-hand sides to solve the inverse NUDFT problem at the cost of an FFT plus some sparse matrix-vector products. We find (see subsection 5.2) that this method works well when the nodes of V are mildly clustered without irregular gaps.

Recently Kircheis and Potts proposed a direct solution via $x \approx V^* \text{diag}(\mu)b$, where the weight vector μ is precomputed by solving a adjoint Vandermonde system of larger size $(2n-1) \times m$ [35, Sec. 3]. The latter enforces that the weights μ_j at nodes p_j form an exact quadrature scheme on $p \in (0, 1)$ for all modes $e^{2\pi i k p}$ with $k = -n+1, \dots, n-1$, which can only in general be consistent when $m \geq 2n-1$. However, to achieve a fast scheme this system must be solved iteratively (again by CG on normal or adjoint normal equations), and in our experience this converges no more reliably than the original NUDFT system.

The direct method for $Vx = b$ that is perhaps closest in spirit to our own work is that of [21]: this evaluates the Lagrange interpolant (cotangent kernel) using a fast multipole method, and is unfortunately limited to the setting where V is square. .

REMARK 2 (Overdetermined vs underdetermined problems). *As the above (and section 5) suggests, the condition number $\kappa_2(V)$ of a problem has a dramatic effect on the relative merits of different algorithms (iterative vs direct). It is thus worth distinguishing three classes of analysis results on $\kappa_2(V)$ in the literature.*

- *When the type-II linear system $Vx = b$ is overdetermined, as in our study, $\kappa_2(V)$ controls the stability of the solution [58, Ch. 15] (loosely, the factor by which $\|x\|$ may exceed $\|b\|$). The absence of gaps in the sampling set $\{p_j\}_{j=1}^m$ appears to guarantee that $\kappa_2(V)$ remain small (see [19], and for Voronoi weighting see [22, Prop. 2] and [1, Lem. 4.2]). Conversely, gaps somewhat larger than the wavelength π/n at the Nyquist frequency $n/2$ appear to lead to ill-conditioning.*
- *For the square case $m = n$, the problem becomes one of interpolation rather than least-squares fitting [21], but $\kappa_2(V)$ still reflects its stability. Recent results show that this is stable when the sample points have deviations from uniformity limited to a fraction of the uniform spacing $1/n$ [2, 65].*
- *For the underdetermined type-II case $m < n$, $Vx = b$ always has a nullspace, so regularization is always needed [38] or one must choose an appropriate minimum-norm solution. However, $\kappa_2(V)$ instead describes the stability of the adjoint (type-I)*

overdetermined linear system $V^*y = b$, interpreted as solving for the n strengths y_k whose type-I transform matches a given set of Fourier coefficients b_j , $j = 1, \dots, m$. This problem is well studied in the superresolution literature, where analysis shows polynomial ill-conditioning associated with clustering of (as opposed to gaps in) the nodes [6, 7, 37]. Here κ_2 is controlled by the minimum (as opposed to maximum) node separation; this class of results has no bearing on the stability of (1.2). Indeed, we will see that clustering does not induce poor conditioning (see Grid 2 below).

1.5. Organization. The rest of the paper is organized as follows: In section 2, we briefly review the connection between low rank approximation and special displacement structures. Then in section 3, we use this framework to explain low rank properties of the transformed matrix C and develop a construction algorithm for an HSS matrix that approximates C well. In section 4, we describe the rectangular HSS solver used in our direct inversion scheme. Numerical experiments are discussed in section 5, starting with a summary of recommendations for which solver to use in which regime. A brief discussion of extensions and future work is given in section 6. The five iterative methods against which we compare are detailed in an appendix.

2. The singular values of matrices with low displacement rank. Our solver makes use of *displacement structure*, a property possessed by many highly structured matrices, including Toeplitz, Cauchy, Hankel, and Vandermonde matrices [9]. A matrix X is said to have (A, B) -displacement structure if it satisfies the Sylvester matrix equation

$$AX - XB = M \quad (2.1)$$

for some low rank matrix M . The rank of M is called the displacement rank of X . As seen in (1.6), C has (Γ, Λ) -displacement structure with a *displacement rank* of 1. Following [9], we use the displacement structure of C to explain its low rank properties. We begin with a brief review of the connection between displacement structure and singular value decay.

Consider the displacement relation (2.1), where A and B are normal matrices. We assume the spectra of A and B are contained by bounded, disjoint sets E_1 and E_2 in the complex plane: $\lambda(A) \subset E_1$ and $\lambda(B) \subset E_2$. It is shown in [9] that

$$\sigma_{k\rho+1}(X) \leq Z_k(E_1, E_2)\|X\|_2, \quad (2.2)$$

where $\text{rank}(M) \leq \rho$, and $Z_k(E_1, E_2)$ is the k th *Zolotarev number* associated with E_1, E_2 , defined to be the solution to a certain rational extremal problem involving E_1 and E_2 . For a detailed overview of Zolotarev numbers in this context, see [9, 60]. When E_1 and E_2 are well-separated, Z_k decays rapidly and we therefore expect that X is of low numerical rank. For our purposes, E_1 and E_2 will always be selected as arcs on the unit circle. The following lemma, restated from [60], is crucial for our results:

LEMMA 2.1. Let $\mathcal{A}_J = \{e^{it} : t \in [\tau_1, \tau_2]\}$, $\mathcal{A}_K = \{e^{it} : t \in [\rho_1, \rho_2]\}$. Then,

$$Z_k(\mathcal{A}_J, \mathcal{A}_K) \leq 4\mu^{-2k}, \quad \mu = \exp\left(\frac{\pi^2}{2\log(16\eta)}\right), \quad (2.3)$$

where

$$\eta = \frac{|\sin((\rho_1 - \tau_1)/2) \sin((\rho_2 - \tau_2)/2)|}{|\sin((\rho_2 - \tau_1)/2) \sin((\rho_1 - \tau_2)/2)|}. \quad (2.4)$$

Proof. See Theorem 8 in [60, Ch. 4]. \square

Bounds on the the singular values of X imply estimates for its so-called ϵ -rank, which is defined as follows:

DEFINITION 2.2. Let $0 < \epsilon < 1$ and $m \geq n$. The ϵ -rank of $X \in \mathbb{C}^{m \times n}$, denoted by $\text{rank}_\epsilon(X)$, is the smallest integer $0 \leq k \leq n-1$ such that $\sigma_{k+1}(X) \leq \epsilon \|X\|_2$.

By definition, if $\text{rank}_\epsilon(X) \leq k$, then there is a rank- k matrix X_k where $\|X - X_k\|_2 \leq \epsilon \|X\|_2$.

2.1. The factored alternating direction implicit method. Intimately related to the Zolotarev numbers is the alternating direction implicit (ADI) method [40, 48] for solving the Sylvester matrix equation (2.1). Setting $X^{(0)} = 0$, each ADI iteration consists of two steps:

1. Solve for $X^{(j+1/2)}$ in $(A - \beta_{j+1}I)X^{(j+1/2)} = X^{(j)}(B - \beta_{j+1}I) + M$.
2. Solve for $X^{(j+1)}$ in $X^{(j+1)}(B - \alpha_{j+1}I) = (A - \alpha_{j+1}I)X^{(j+1/2)} - M$.

After k iterations, an approximation $X^{(k)} \approx X$ is constructed. Convergence of the method depends on the choice of *shift parameters* $\{\alpha_j, \beta_j\}_{j=1}^k$. The shift parameters that minimize the error after k iterations are given by the zeros and poles of a type (k, k) rational function that solves an optimization problem on the spectral sets $\lambda(A)$ and $\lambda(B)$ known as Zolotarev's third problem [31, 40, 66]. When optimal shift parameters are used and we let E_1, E_2 serve as stand-ins for the spectral sets that they contain, one can show that [57]

$$\|X - X^{(k)}\|_2 \leq Z_k(E_1, E_2) \|X\|_2.$$

In our case, E_1, E_2 are always arcs on the unit circle. The optimal shift parameters for this case are known and can be computed at a trivial cost [60, Ch. 1] using elliptic functions.

A mathematically equivalent version of ADI called factored ADI (fADI) [10, 41] constructs the solution $X^{(k)}$ in the form of a low rank decomposition $X^{(k)} = ZW^*$, where Z, W each have $k\rho$ columns. It uses as input a factorization $M = FG^*$, where $F \in \mathbb{C}^{m \times \rho}$, $G \in \mathbb{C}^{m \times \rho}$. The fADI algorithm is our primary engine for constructing low rank approximations to submatrices of C . The cost of this method depends on the cost for shifted matrix-vector products $z \mapsto (M + \gamma I)z$ and shifted inverts $z \mapsto (M + \gamma I)^{-1}z$ for $M \in \{A, B\}$. In our case, A and B will always be diagonal, so the cost for applying k iterations of fADI on a $p \times q$ submatrix of C is only $\mathcal{O}((p+q)k)$ operations. A detailed overview of the connection between Zolotarev numbers and ADI, including pseudocode for the fADI algorithm, can be found in [57, 60].

3. The low rank properties of C . As shown in (1.6), the matrix C has (Γ, Λ) displacement structure with displacement rank 1. Since Γ and Λ potentially have interlaced (and possibly coinciding) eigenvalues, (1.6) is typically not useful for understanding the singular values of the entire matrix C . However, (1.6) can be used to show that certain *submatrices* of C have low numerical rank. Throughout, we use the notation C_{JK} to denote the submatrix of C with rows indexed by members of set J and columns indexed by members of set K .

We begin with an example. Suppose the index sets are $J = \{q+1, q+2, \dots, m\}$ and $K = \{1, 2, \dots, p\}$, so that C_{JK} is a submatrix in the lower left corner of C . By (1.6),

$$\Gamma_J C_{JK} - C_{JK} \Lambda_K = (uv^*)_{JK}, \quad (3.1)$$

where $\Gamma_J = \text{diag}(\gamma_{q+1}, \dots, \gamma_m)$ and $\Lambda_K = \text{diag}(\omega^2, \dots, \omega^{2p})$. Choose arcs \mathcal{A}_J and \mathcal{A}_K so that $\lambda(\Gamma_J) \subset \mathcal{A}_J$, $\lambda(\Lambda_K) \subset \mathcal{A}_K$. Whenever these two arcs do not overlap, Lemma 2.1 shows that the singular values of C_{JK} decay rapidly. Indeed, by (2.2) and Lemma 2.1,

$$\sigma_{k+1}(C_{JK}) \leq 4\mu^{-2k} \|C_{JK}\|_2,$$

which implies bounds on $\text{rank}_\epsilon(C_{JK})$. Moreover, we can use fADI to efficiently construct a low rank approximation to C_{JK} that achieves these estimates. This gives us a scheme for

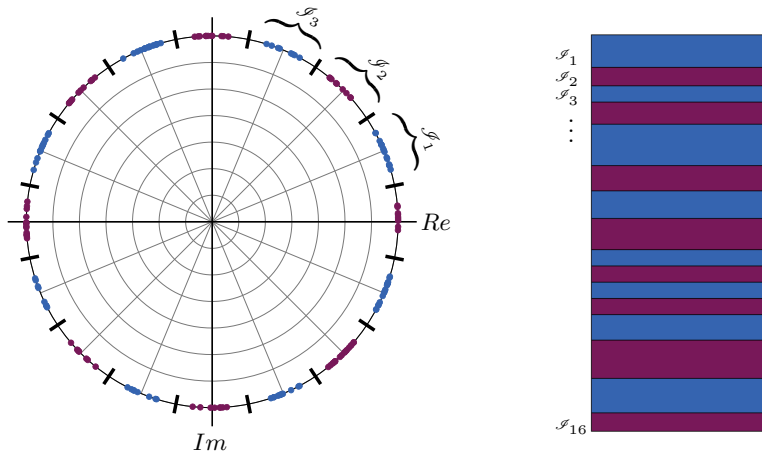


Fig. 1: *Left*: The unit circle is split into $n = 16$ regions. At the center of each region is the root of unity $\omega^{2\kappa}$, and each region is associated with a subset of nodes (blue and magenta points) that are indexed by the cluster \mathcal{S}_κ . Each cluster indexes those nodes γ_j between $\omega^{2\kappa \pm 1}$. *Right*: A cartoon portrayal of the $m \times n$ matrix C associated with these nodes, partitioned into n slabs. The number of rows in each slab corresponds to the size of the associated cluster. Our HSS approximation to C works with these slabs instead of individual rows.

compressing submatrices of C that are of low numerical rank. In the rest of this section, we use these methods to describe the hierarchical rank structure of C and construct a rank-structured approximation $H \approx C$.

3.1. A geometric perspective. Not every submatrix of C is compressible. However, C always contains some collection of submatrices with small ϵ -rank. The locations and dimensions of these submatrices depends on the distribution of the nodes $\{\gamma_j\}_{j=1}^m$ of the Vandermonde matrix V on the unit circle. In an extreme example where all of the nodes are clustered between two adjacent roots of unity, C is a low rank matrix. For less extreme cases, we seek a general strategy for recursively partitioning C into a collection of compressible submatrices. To do this, we organize the partitioning around subsets of nodes that we index using *clusters*.

DEFINITION 3.1. *For $1 \leq \kappa \leq n$, the cluster \mathcal{S}_κ consists of all j such that*

$$\gamma_j \in \{\exp(2\pi it/n) : \kappa - 1/2 < t \leq \kappa + 1/2\}.$$

Each cluster \mathcal{S}_κ gives rise to a slab of rows of C (see Figure 1). The use of slabs allows us to essentially treat C as if it were square for the purposes of partitioning, as there are n columns of C and n slabs of rows. It is possible for some clusters to be empty, and in extreme cases where a single cluster is unusually large, we modify the row partitioning and assign excess rows to neighboring clusters³. In the next section, we apply standard hierarchical partitioning strategies to C with slabs replacing rows. Then, in subsection 3.4, we bound the ϵ -ranks of relevant submatrices that arise in these partitions.

³The consequence is that in our automated construction of the HSS approximation to C , certain diagonal blocks that are treated as full rank may actually have low numerical rank.

3.2. HODLR matrices. With a slight abuse of terminology, we say that C is a *HODLR* (*hierarchical off-diagonal low rank*) matrix if it can be divided into blocks

$$C = \begin{bmatrix} D_\ell & A_{\ell r} \\ A_{r\ell} & D_r \end{bmatrix}, \quad (3.2)$$

where (i) the off-diagonal blocks $A_{\ell r}$ and $A_{r\ell}$ are well-approximated by low rank matrices and (ii) the diagonal blocks D_ℓ and D_r can be recursively partitioned to have the same form as (3.2). The partitioning is repeated recursively until a minimum block size is reached. For us, the matrices D_ℓ and D_r are rectangular, and the number of rows in each depends on how the nodes are clustered.

Let us be more precise about this structure. We associate the HODLR matrix with a binary tree \mathcal{T} whose vertices we label by a post-order traversal: We label the root as 0 and the children of $t \in \mathcal{T}$ by $2t+1$ and $2t+2$ (see Figure 2). To each vertex $t \in \mathcal{T}$, we associate a set of column indices K_t such that (i) $K_0 = \{1, \dots, n\}$, (ii) each block of indices is contiguous, i.e., $K_t = \{\kappa_1, \kappa_1+1, \dots, \kappa_2\}$ for some $1 \leq \kappa_1 \leq \kappa_2 \leq n$, and (iii) each parent is the disjoint union of its children, i.e., $K_t = K_{2t+1} \cup K_{2t+2}$. We then define J_t to be a union of the clusters $\kappa \in K_t$, i.e., $J_t := \bigcup_{\kappa \in K_t} \mathcal{I}_\kappa$. We refer to $D_t := C_{J_t K_t}$ as a *diagonal* HODLR block. The blocks $A_{r\ell} := C_{J_r K_\ell}$ and $A_{\ell r} := C_{J_\ell K_r}$ are called *off-diagonal* HODLR blocks. An example with multiple levels is shown in Figure 2. As we prove in subsection 3.4, the off-diagonal blocks $A_{\ell r}$ and $A_{r\ell}$ have low (numerical) rank at every level of the tree.

In the special case where $m = n$ and each \mathcal{I}_κ contains exactly one node, the cluster-based HODLR structure we use is equivalent to the usual HODLR structure for square matrices associated with perfectly balanced binary trees [15,43]. This corresponds to sample points p_j with bounded jitter relative to the equispaced case, that is $|p_m - (m-j)/m| < 1/2m$ for $j = 1, \dots, m$. However, in general, our paradigm allows for rectangular matrices with uneven divisions of rows at any fixed level of the tree (see Figure 2).

One could use fADI to construct low rank approximations to every relevant off-diagonal block in C , and then apply a solver that exploits HODLR structure to approximately solve $Cy = b$. However, we do not fully explore this possibility because, in addition to HODLR structure, C possesses further structure can be exploited for greater efficiency. We build on the HODLR properties of C to describe these structures in the next section.

3.3. HSS matrices. In the HODLR form, each diagonal block D_t (corresponding to a parent t with children ℓ and r) has the recursive form

$$D_t = \begin{bmatrix} D_\ell & A_{\ell r} \\ A_{r\ell} & D_r \end{bmatrix}.$$

and we assume no relation between the off-diagonal blocks $A_{\ell r}$ and $A_{r\ell}$ across different levels of \mathcal{T} . A HODLR matrix is said to have *HSS structure* [15] if the off-diagonal blocks are related in the following (recursive) way: If $t \in \mathcal{T}$ is not a root or leaf and t has children ℓ and r , then

$$D_t = \begin{bmatrix} D_\ell & A_{\ell r} \\ A_{r\ell} & D_r \end{bmatrix} = \begin{bmatrix} D_\ell & U_\ell B_{\ell r} V_r^* \\ U_r B_{r\ell} V_\ell^* & D_r \end{bmatrix}, \quad (3.3)$$

where the *basis matrices* U_t and V_t are related across levels of the tree by relations

$$U_t = \begin{bmatrix} U_\ell & 0 \\ 0 & U_r \end{bmatrix} \begin{bmatrix} R_{\ell t} \\ R_{rt} \end{bmatrix}, \quad V_t = \begin{bmatrix} V_\ell & 0 \\ 0 & V_r \end{bmatrix} \begin{bmatrix} W_{\ell t} \\ W_{rt} \end{bmatrix}. \quad (3.4)$$

This structure is analogous to the structure of the standard square HSS matrix (closely related to the \mathcal{H}^2 structure [28]), except that the diagonal blocks are rectangular with dimensions

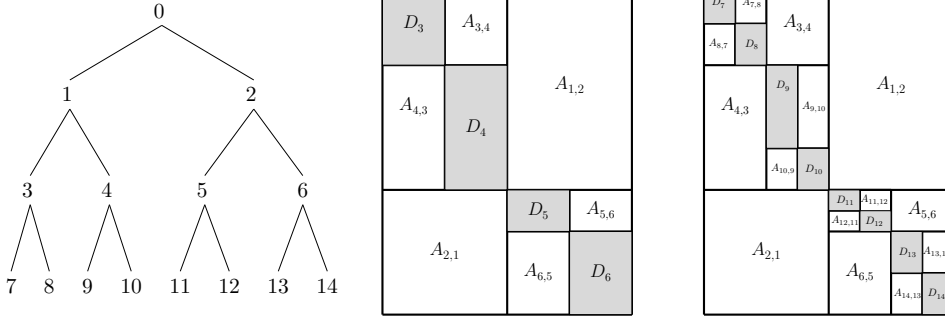


Fig. 2: A HODLR matrix is recursively partitioned into off-diagonal blocks associated with the tree \mathcal{T} (left). Blocking associated with the first two levels of the tree are shown in the middle, and blocking associated with first three levels is shown on the right. Each of the off-diagonal blocks $A_{\ell r}$ is low rank. If the conditions in (3.3) and (3.4) also hold, we say H has HSS structure.

determined via the HODLR tree for C , which in turn is based on the clusters associated with C . The recursions (3.3) and (3.4) allow the entire matrix $C = D_0$ to be assembled from the following generator matrices:

- Leaf generators: D_t, U_t , and V_t for each leaf node $t \in \mathcal{T}$.
- Parent-child generators: R_{ct} and W_{ct} for every parent $t \in \mathcal{T}$ with child c .
- Sibling generators: $B_{\ell r}$ for every pair of siblings ℓ and r .

3.3.1. HSS rows and columns. The construction of the generator matrices requires finding U_t and V_t at each level so that they are *nested* in the sense that if t has children ℓ and r , the first rows of U_t are spanned by U_ℓ , with the rest of U_t 's rows are spanned by U_r . To do this, we work with the *HSS rows* and *HSS columns* of the matrix C .

An HSS column of C associated with $t \in \mathcal{T}$ is formed by selecting a strip of contiguous columns K_t and excluding the rows in J_t . We denote this as $A_t^{\text{col}} = C(J_t^c, K_t)$ where $J_t^c = J_0 \setminus J_t$ denotes the complement of J_t defined in subsection 3.2. One can similarly define the HSS row $A_t^{\text{row}} = C(J_t, K_t^c)$. Figure 3 displays some HSS rows and columns.

If the maximum rank of any HSS block row or column in C is k , then there exists a set of off-diagonal generators $\{U_t, V_t, R_{ct}, W_{ct}, B_{\ell r}\}$ where each generator has at most k columns. By storing only the generators, the HSS matrix can be represented using only $\mathcal{O}((m+n)k)$ storage. Using an interpolative decomposition method [17] further reduces the storage cost since each $B_{\ell r}$ is a submatrix of C and can therefore be stored via a small list of indices. In practice, the rank of the off-diagonal leaf generator matrices are selected adaptively, so k can vary for each leaf node.

With these definitions in place, we can describe the rank structure of the transformed NUDFT matrix $C = VF^*$, along with an algorithm that constructs the HSS generators. We then describe a solver based on these generators in Section 4.

3.4. The rank structure of C . The next theorem shows⁴ that the ϵ -ranks of the HSS columns and rows of C only grow like $\mathcal{O}(\log(n) \log(1/\epsilon))$. The ϵ -ranks of every off-diagonal HODLR block in C behave similarly.

⁴The authors express gratitude to Bernhard Beckermann, who independently derived a proof similar in structure to this one in the context of Toeplitz matrices in 2018. Work related to this is found in [60, Ch. 4].

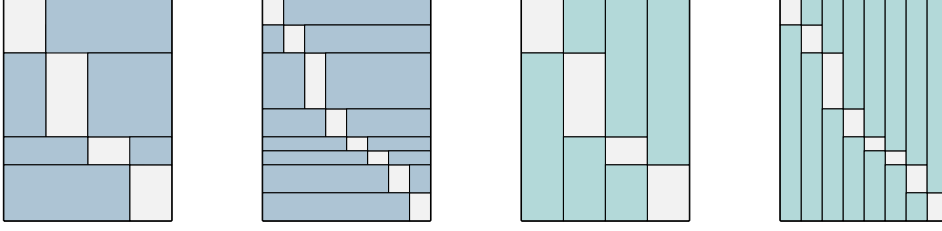


Fig. 3: Example HSS rows (blue, *left*) and HSS columns (teal, *right*) of C are shown for two different levels of \mathcal{T} . The gray rectangular blocks are excluded from the submatrices.

THEOREM 3.2. *Let $C \in \mathbb{C}^{m \times n}$ be as in (1.6). If A is an HSS column or row of C (or a submatrix of such a column or row), then*

$$\text{rank}_\epsilon(A) \leq \left\lceil \frac{2 \log(4/\epsilon) \log(4n)}{\pi^2} \right\rceil. \quad (3.5)$$

Proof. The proofs for HSS rows and columns are similar, so we consider the case of an HSS column. Consider an HSS column $A_t^{\text{col}} = C_{J_t^c K_t}$, where

$$K_t = \{\kappa_1, \kappa_1 + 1, \dots, \kappa_2\} \quad \text{and} \quad J_t^c = \{1 \leq j \leq m : j \notin \mathcal{J}_\kappa \text{ for every } \kappa_1 \leq \kappa \leq \kappa_2\}.$$

Let $A = C_{JK}$ be any submatrix of A_t^{col} where $K \subset K_t$ and $J \subset J_t^c$. Let $\Gamma_J = \text{diag}(\gamma_j)_{j \in J}$ and $\Lambda_K = \text{diag}(\omega^{2\kappa})_{\kappa \in K}$. By (1.6), we observe that

$$\text{rank}(\Gamma_J A - A \Lambda_K) = 1.$$

From (2.2), we have that for $1 \leq k \leq \min(|J|, |K|) - 1$,

$$\sigma_{k+1}(A) \leq Z_k(\mathcal{A}_J, \mathcal{A}_K) \|A\|_2,$$

where \mathcal{A}_J and \mathcal{A}_K are arcs on the unit circle that contain $\lambda(\Gamma_J)$ and $\lambda(\Lambda_K)$, respectively:

$$\begin{aligned} \mathcal{A}_J &= \{e^{i\theta} : \pi(2\kappa_2 + 1)/n \leq \theta \leq \pi(2n + 2\kappa_1 - 1)/n\}, \\ \mathcal{A}_K &= \{e^{i\theta} : 2\pi\kappa_1/n \leq \theta \leq 2\pi\kappa_2/n\}. \end{aligned}$$

Applying Lemma 2.1, we have that

$$\sigma_{k+1}(A) \leq 4\mu^{-2k} \|A\|_2, \quad \mu = \exp\left(\frac{\pi^2}{2 \log(16\eta)}\right), \quad (3.6)$$

where

$$\eta = \frac{\sin^2\left(\frac{\pi}{n}(\kappa_2 - \kappa_1) + \frac{\pi}{2n}\right)}{\sin^2\left(\frac{\pi}{2n}\right)} \leq n^2. \quad (3.7)$$

The upper bound on η follows from the fact that $\sin(\pi/2n) \geq 1/n$ for $n \geq 1$. Substituting (3.7) into (3.6), rearranging, and using the definition of ϵ -rank establishes (3.5). \square

We remark that in some extreme cases, an HSS row or column may have dimensions such that its mathematical rank is less than the bound given in Theorem 3.2 on the ϵ -rank. Also, tighter bounds can be established for the submatrices of A_t^{col} (or A_t^{row}), including HODLR blocks of C , if one works directly with the parameters defining the particular submatrices.

3.5. Constructing the generators. [Theorem 3.2](#) establishes that the HSS rows and columns have low numerical rank, which implies that there exists a matrix $H \approx C$ for which each HSS row or column of H is a low rank approximation to the corresponding submatrix of C . We use a fADI-based interpolative decomposition method [60, Ch.4] to cheaply construct the generators associated with H . We illustrate the idea using an HSS row. Let t be a leaf node of \mathcal{T} and let A_t^{row} be the t th HSS row of C . Assume A_t^{row} has m_t rows and $n - n_t$ columns, with $n_t \sim \log n$. We assume at this level that m_t is $\mathcal{O}(\log m)$. Applying fADI directly, one would construct the low rank approximation $ZW^* \approx A_t^{\text{row}}$, where Z is a small matrix of size $m_t \times k$, and W is tall and thin, of size $n - n_t \times k$. However, it is wasteful and costly to construct W . Fortunately, fADI constructs Z and W independently [60, Ch.4], and there is no need to construct W or touch the long dimension of A_t^{row} at all in order to construct Z . With Z in hand, we do a column-pivoted QR decomposition of Z^T to find

$$Z = \mathcal{P}\mathcal{R}^T\mathcal{Q}^T, \quad R^T = \begin{bmatrix} R_a^T \\ R_b^T \end{bmatrix}$$

where \mathcal{P} is a permutation matrix, $\mathcal{R}^T \in \mathbb{C}^{m_t \times k}$ is lower triangular with k columns, $\mathcal{Q} \in \mathbb{C}^{k \times k}$ is unitary, and R_a^T is of size $k \times k$. This decomposition is then used in a standard way to construct the one-sided interpolative decomposition [17, 44]

$$A_t^{\text{row}} = U_t A_t^{\text{row}}(S_t^{\text{row}}, :), \quad U_t = \mathcal{P} \begin{bmatrix} I_k \\ R_b^T R_a^{-T} \end{bmatrix},$$

where I_k is the $k \times k$ identity matrix and S_t^{row} indexes a subset of rows corresponding to the top k rows selected by \mathcal{P} . We store the leaf generator basis matrix U_t and the index set S_t^{row} . We call the subselected rows indexed by S_t^{row} *basis rows*. A similar process is applied to HSS columns to construct each of the leaf generator basis matrices V_t and select basis columns indexed by S_t^{col} . The sibling generators at this level are then simply given by $B_{\ell r} = C(S_\ell^{\text{row}}, S_r^{\text{col}})$.

Once the leaf generators are constructed, we move one level up \mathcal{T} . For each parent $t \in \mathcal{T}$ at this level, we must construct the left and right parent-child generators $R_{\ell t}$ (R_{rt} resp.) and $W_{\ell t}$ (W_{rt} resp.), as well as sibling generators. We do this by applying fADI-based one-sided interpolative decompositions on the basis rows or basis columns of the appropriate children, and note that then number of basis rows (columns) is $< 2k$, where k is the maximum rank of any HSS row or column at the leaf level. In total, the interpolative fADI-based compression strategy constructs the generators for $H \approx C$ in $\mathcal{O}(mk^2) = \mathcal{O}(m \log^2(n) \log^2(1/\epsilon))$ operations. With $H \approx C$ constructed, we have completed step 2 in [Algorithm 1.1](#). We now turn to step 3 and develop an efficient rank-structured solver.

4. A hierarchically semiseparable least-squares solver. We now present an algorithm that approximately solves the problem

$$y = \underset{y \in \mathbb{C}^n}{\operatorname{argmin}} \|Hy - b\|_2^2, \quad (4.1)$$

The developments in this section are general, applying to an arbitrary HSS matrix $H \in \mathbb{C}^{m \times n}$ and vector $b \in \mathbb{C}^m$. Throughout this section, let k be the maximum rank of the HSS rows and columns of H . For the inverse NUDFT problem, we demonstrated in [section 3](#) that one can construct an HSS matrix H where $C \approx H$ with $k = \mathcal{O}(\log(n) \log(1/\epsilon))$. Up to the approximation $H \approx C$, the least-squares problem (4.1) is equivalent to the inverse NUDFT problem (1.2) with $y = Fx$.

4.1. Solutions via the normal equations. A natural first approach to the least-squares problem (4.1) is to work with the normal equations $(H^*H)y = H^*b$, a linear system involving the square HSS matrix H^*H . Indeed, the maximum rank of an HSS row or column in H^*H is $2k$ and the HSS generators for H^*H can be found in $\mathcal{O}(mk^2)$ operations. At that point, any number of fast direct solvers [45, 50, 63] can be applied to solve the normal equations. Relatedly, one may start with $Vx = b$ and observe that V^*V is Toeplitz. Fast direct solvers for Toeplitz matrices are available [60, 64], so one must only implicitly form V^*V in such a way that these solvers can be applied to solve (1.1) via the normal equations. We make comparisons with such an algorithm in our numerical experiments in section 5.

The problem with these methods is that they square the condition number of the problem: solving the normal equations explicitly can result in lower accuracy than a dedicated least-squares solver. In our setting, we expect that $\kappa_2(H)$ is already large and want to avoid exacerbating the issue. We remark that one can reduce the HSS least-squares problem to an HSS linear system without squaring the condition number (see subsection 6.1), though the $\mathcal{O}((m/n)^2 \cdot mk^2)$ operation cost is not competitive with our direct least-squares solver.

4.2. A direct least-squares solver. Due to the above issues, we avoid the normal equations and work directly with H . Our algorithm is based on the URV factorization algorithm introduced in [62] for solving least-squares problems involving Toeplitz matrices. While that solver takes advantage of additional structure related to Toeplitz matrices, its URV factorization method is generalizable, and we present such a generalization here. The URV factorization is so-named because it decomposes a rectangular HSS matrix into the factors U , R , and V , with U and V being a product of unitary matrices and R being upper triangular. These factors are never constructed or stored explicitly, but can instead be represented by sequences of sparse blocks in a hierarchical structure. The blocks are then used to reduce the linear system into a collection of small triangular systems that can be solved efficiently. The method is analogous to solution of least-squares problems by QR factorization, but is modified to exploit hierarchical structures.

An important difference between the present work and [62] is the size of the blocks. In [62], the rectangular diagonal blocks at each level of \mathcal{T} are uniform or close to uniform in size. In our case, the block sizes are determined by the clustering patterns of the nodes. They can vary substantially from vertex to vertex in \mathcal{T} , and short-fat rectangular diagonal blocks inevitably arise⁵. While our method for constructing H relies on the displacement structure of C , our solver is completely general and can be used for any HSS matrix.

An essential ingredient in our solver is the *size reduction* step, introduced by [62]. The size reduction step applies unitary transformations to introduce additional zeros at each stage of the algorithm, controlling the *rectangularity* (ratio of rows to columns) during recursive stages of the algorithm. We begin with the URV factorization.

4.3. Factorization. The algorithm proceeds by traversing the HSS tree beginning with the leaves and continuing until the root is reached. Before diving into the algorithm, we establish some notation. For each $t \in \mathcal{T}$, the *tth block row* are the rows of H indexed by J_t and the *tth block column* are the columns indexed by K_t . Observe that, the *tth block row* contains the diagonal block D_t and the HSS row A_t^{row} as complementary submatrices, and likewise for the *tth block column*. For a leaf $t \in \mathcal{T}$, we denote m_t (resp. n_t) as the number of rows (resp. columns) in the *tth block row* (resp. column). As a notational convenience, we assume all generators (except D_t) have exactly k columns; this restriction is not necessary in practice.

⁵The algorithm is breakdown-free as long as each block is of size $\tilde{m}_k \times n_t$, with $n_t - k \leq \tilde{m}_k$. This is a significantly more mild condition than that all of the blocks are thin, i.e., $n_t \leq m_k$.

Begin at each leaf $t \in \mathcal{T}$. The first step is the *size reduction* step, designed to control the number of rows relative to columns in subsequent steps of the algorithm. The size reduction step introduces zeros at the bottom of U_t and D_t by means of a QR decomposition

$$[U_t \ D_t] = \Omega_t \begin{bmatrix} k & n_t \\ \tilde{U}_t & \tilde{D}_t \\ 0 & 0 \end{bmatrix} \begin{array}{l} k + n_t \\ m_t - k - n_t \end{array},$$

where $\Omega_t \in \mathbb{C}^{(k+n_t) \times (k+n_t)}$ is unitary. When we multiply the t th block row of H by Ω_t^* , it zeroes out many of the rows in that block, allowing us to ignore these rows in future steps of the algorithm. This size reduction step only needs to be performed if $[U_t \ D_t]$ has many more rows than columns; using the factor 6 as cutoff produces good results in our experiments. We denote the number of rows of \tilde{U}_t, \tilde{D}_t as \tilde{m}_t .

We now work with the reduced leaf generators \tilde{U}_t, \tilde{D}_t , and V_t to compute the URV factorization as in [62]. Useful diagrams related to this process in the Toeplitz setting are given in [62, Fig. 2.3]. The first step introduces zeros into V_t by means of a *reversed QR factorization*:

$$V_t = P_t \begin{bmatrix} n_t \\ 0 \\ \bar{V}_t \end{bmatrix} \begin{array}{l} n_t - k \\ k \end{array},$$

where $\bar{V}_t = [\triangleleft]$ is *antitriangular*, $(\bar{V}_t)_{j\kappa} = 0$ if $j + \kappa < k + 1$, and $P_t \in \mathbb{C}^{n_t \times n_t}$ is unitary. Such a factorization can be obtained by computing a QR factorization of V_t , reversing the order of the columns of the first factor, and reversing the order of the rows of the second factor. Multiplying the t th block column by P_t has the effect of zeroing out many columns of the HSS column A_t^{col} . The modified diagonal block $\hat{D}_t = \tilde{D}_t P_t$ is dense, so we introduce as many zeros as possible by a partial triangularization. Partition the diagonal block as:

$$\hat{D}_t = \tilde{D}_t P_t = \begin{bmatrix} n_t - k & k \\ \hat{D}_{t;11} & \hat{D}_{t;12} \\ \hat{D}_{t;21} & \hat{D}_{t;22} \end{bmatrix} \begin{array}{l} n_t - k \\ \tilde{m}_t - n_t + k \end{array}.$$

Now, introduce zeros in \hat{D}_t by means of a QR factorization:

$$\begin{bmatrix} \hat{D}_{t;11} \\ \hat{D}_{t;21} \end{bmatrix} = Q_t \begin{bmatrix} n_t - k \\ \bar{D}_{t;11} \\ 0 \end{bmatrix} \begin{array}{l} n_t - k \\ \tilde{m}_t - n_t + k \end{array},$$

where $Q_t \in \mathbb{C}^{\tilde{m}_t \times \tilde{m}_t}$ is unitary. Now multiply \hat{D}_t by Q_t^* . This results in a modified diagonal block

$$\bar{D}_t = Q_t^* \hat{D}_t = \begin{bmatrix} n_t - k & k \\ \bar{D}_{t;11} & \bar{D}_{t;12} \\ 0 & \bar{D}_{t;22} \end{bmatrix} \begin{array}{l} n_t - k \\ \tilde{m}_t - n_t + k \end{array}$$

and modified leaf generator matrix

$$\bar{U}_t = Q_t^* \tilde{U}_t = \begin{bmatrix} k \\ \bar{U}_{t;1} \\ \bar{U}_{t;2} \end{bmatrix} \begin{array}{l} n_t - k \\ \tilde{m}_t - n_t + k \end{array}.$$

The new diagonal block \overline{D}_t is now almost triangular. The sticking point is the (2, 2)-block $\overline{D}_{t;22}$. If we truncate the t th block row so that the rows coinciding with $\overline{D}_{t;22}$ are not included, then the remaining block row is upper triangular. This completes the factorization at the leaf level. We then handle $\overline{D}_{t;22}$ recursively.

For a non-leaf $t \in \mathcal{T}$ with children ℓ and r , define

$$D'_t = \begin{bmatrix} \overline{D}_{\ell;22} & \overline{U}_{\ell;2} B_{\ell,r} \overline{V}_r^* \\ \overline{U}_{r;2} B_{r,\ell} \overline{V}_\ell^* & \overline{D}_{r;22} \end{bmatrix}, \quad U'_t = \begin{bmatrix} \overline{U}_{\ell;2} R_{\ell,t} \\ \overline{U}_{r;2} R_{r,t} \end{bmatrix}, \quad V'_t = \begin{bmatrix} \overline{V}_\ell W_{\ell,t} \\ \overline{V}_r W_{r,t} \end{bmatrix},$$

Here, $B_{\ell,r}$, $B_{r,\ell}$, $R_{\ell,t}$, $R_{r,t}$, $W_{\ell,t}$, and $W_{r,t}$ refer to the sibling and parent-child generators for the HSS matrix H , defined in [subsection 3.3](#). If t is not the root, we perform the same sequence of operations we performed for the leaf nodes, using D'_t , U'_t , and V'_t in place of D_t , U_t , and V_t using m_t and n_t to denote the number of rows and columns of D'_t , respectively. If t is the root, we only need to perform a QR decomposition

$$D'_0 = Q_0 \begin{bmatrix} \overline{D}_{0;11} & \\ & 0 \end{bmatrix} \begin{matrix} m_0 \\ n_0 - m_0 \end{matrix},$$

where $Q_0 \in \mathbb{C}^{m_0 \times m_0}$ is unitary. The matrix D'_0 is small, so this QR decomposition is inexpensive. A summary description is shown in [Algorithm 4.1](#). Once the blocks comprising the URV factors are computed, we are ready to solve the least-squares problem.

4.4. Solution. We break the procedure for solving the least-squares problem into two large steps. The first involves transforming the right-hand side, and the second uses backsubstitution to solve a sequence of hierarchical triangular systems.

4.4.1. Apply unitary operations Q_t^* and Ω_t^* to the right-hand side. The URV triangularization process modifies the rows of the linear system, and we must account for that in the right-hand side. Let b_t denote the block of the right-hand side of b consisting of those rows associated with $t \in \mathcal{T}$. Beginning with each leaf node t , we define

$$c_t = \begin{bmatrix} Q_t^* & 0 \\ 0 & I \end{bmatrix} \Omega_t^* b_t = \begin{bmatrix} c_{t;1} \\ c_{t;2} \\ c_{t;3} \end{bmatrix} \begin{matrix} n_t - k \\ \tilde{m}_t - n_t + k \\ m_t - \tilde{m}_t \end{matrix}.$$

If the size reduction step was omitted, then one only needs to multiply by Q_t^* :

$$c_t = Q_t^* b_t = \begin{bmatrix} c_{t;1} \\ c_{t;2} \end{bmatrix} \begin{matrix} n_t - k \\ \tilde{m}_t - n_t + k \end{matrix}.$$

Next consider each parent t with children ℓ and r . If t is not the root, then we set $b'_t = [c'_{\ell;2} \quad c'_{r;2}]^T$ and apply the same procedure as we did the leaves, using b'_t in place of b_t . If t is the root, we simply set $c_t = [c_{\ell;2} \quad c_{r;2}]^T$.

4.4.2. Solving the hierarchical triangular system. We now perform a top-down traversal of \mathcal{T} . Beginning with the root 0, solve the triangular system

$$\overline{D}_{0;11} y_0 = c_{0;1}.$$

For the children ℓ and r of 0, partition the solution as $y_0 = [w_{\ell;2} \quad w_{r;2}]^T$ for $w_{\ell;2}, w_{r;2} \in \mathbb{C}^k$ and set $z_\ell = B_{\ell,r} \overline{V}_r^* w_{r;2}$, $z_r = B_{r,\ell} \overline{V}_\ell^* w_{\ell;2}$.

Algorithm 4.1 URV factorization for HSS matrix A

```

1: procedure URV( $t$ ) ▷  $t \in \mathcal{T}$  a node in the HSS tree
2:   if  $t$  not leaf then
3:      $\ell \leftarrow t.\text{left}, r \leftarrow t.\text{right}$ 
4:     Perform recursive calls URV( $\ell$ ) and URV( $r$ )
5:      $D_t \leftarrow \begin{bmatrix} \overline{D}_{\ell;22} & \overline{U}_{\ell;2} B_{\ell,r} \overline{V}_r^* \\ \overline{U}_{r;2} B_{r,\ell} \overline{V}_\ell^* & \overline{D}_{\ell;22} \end{bmatrix}, U_t \leftarrow \begin{bmatrix} \overline{U}_{\ell;2} R_{\ell,p} \\ \overline{U}_{r;2} R_{r,p} \end{bmatrix}, V_t \leftarrow \begin{bmatrix} \overline{V}_\ell W_{\ell,p} \\ \overline{V}_r R_{r,p} \end{bmatrix}$ 
6:   end if
7:   if  $t$  is root then
8:      $\left( Q_t, \begin{bmatrix} \overline{D}_{t;11} \\ 0 \end{bmatrix} \right) \leftarrow \text{QR}(D_t)$ 
9:   else
10:    if  $\text{SIZE}(\begin{bmatrix} U_t & D_t \end{bmatrix}, 2) \geq \text{srf} \cdot \text{SIZE}(U_t, 1)$  then ▷ We used  $\text{srf} = 6$ 
11:       $\left( \Omega_t, \begin{bmatrix} \tilde{U}_t & \tilde{D}_t \\ 0 & 0 \end{bmatrix} \right) \leftarrow \text{QR}(\begin{bmatrix} U_t & D_t \end{bmatrix})$ 
12:    else
13:       $\Omega_t \leftarrow [], \tilde{D}_t \leftarrow D_t, \text{ and } \tilde{U}_t \leftarrow U_t$ 
14:    end if
15:     $(P_t, \text{tmp}) \leftarrow \text{QR}(V_t)$ 
16:     $P_t = P_t(:, \text{end} : -1 : 1), \overline{V}_t \leftarrow \text{tmp}(\text{SIZE}(V_t, 2) : -1 : 1, :)$  ▷ Reversed QR
17:     $\begin{bmatrix} \hat{D}_{t;11} & \hat{D}_{t;12} \\ \hat{D}_{t;21} & \hat{D}_{t;22} \end{bmatrix} \leftarrow \tilde{D}_t P_t$ 
18:     $\left( Q_t, \begin{bmatrix} \overline{D}_{t;11} \\ 0 \end{bmatrix} \right) \leftarrow \text{QR} \left( \begin{bmatrix} \hat{D}_{t;11} \\ \hat{D}_{t;21} \end{bmatrix} \right)$ 
19:     $\begin{bmatrix} \overline{D}_{t;12} \\ \overline{D}_{t;22} \end{bmatrix} \leftarrow Q_t^* \begin{bmatrix} \hat{D}_{t;12} \\ \hat{D}_{t;22} \end{bmatrix}, \begin{bmatrix} \overline{U}_{t;1} \\ \overline{U}_{t;2} \end{bmatrix} \leftarrow Q_t^* \tilde{U}_t$ 
20:  end if
21: end procedure

```

For a non-parent node t , we solve the triangular system

$$\overline{D}_{t;11} w_{t;1} = c_{t;1} - \overline{D}_{t;12} w_{t;2} - \overline{U}_{t;1} z_t$$

and define

$$y_t = P_t \begin{bmatrix} w_{t;1} \\ w_{t;2} \end{bmatrix}.$$

If t is a non-leaf with children ℓ and r , then partition $y_t = \begin{bmatrix} w_{\ell;2} & w_{r;2} \end{bmatrix}^T$ for $w_{\ell;2}, w_{r;2} \in \mathbb{C}^k$ and set

$$z_\ell = B_{\ell,r} \overline{V}_r^* w_{r;2} + R_{\ell,t} z_t, \quad z_r = B_{r,\ell} \overline{V}_\ell^* w_{\ell;2} + R_{r,t} z_t.$$

Conclude by assembling y from all y_t at leaf nodes t .

4.5. Computational costs. To get a representative operation count for the URV factorization, we make the assumption that all the diagonal blocks D_t at the leaf level have $2k$ columns and $2(m/n)k$ rows and that all non-diagonal HSS generators have exactly k columns (in practice, the number of columns for each generator will vary and is determined adaptively according to [Theorem 3.2](#)). This gives an overall cost for the URV factorization step of

$$32mk^2 + 124nk^2 \text{ operations.} \tag{4.2}$$

This is on the same asymptotic order as the HSS factorization step (Step 2 in [Algorithm 1.1](#)), but involves larger constants and is the most expensive step in the algorithm. Once the URV factorization is computed, each subsequent triangular solve is cheaper, requiring just $\mathcal{O}(mk)$ operations. From [Theorem 3.2](#), we have that $k = \mathcal{O}(\log n \log 1/\epsilon)$. The results of the dedicated URV solver compare favorably to the approach using the expanded equations mentioned in [Footnote 11](#), which requires $\mathcal{O}((m/n)^2 \cdot mk^2)$ and pays a quadratic premium in the *rectangularity* $\lceil m/n \rceil$.

5. Numerical experiments. We compare the performance of the proposed ADI-based inverse NUFT solver with several other solvers. As our experiments reflect, the optimal method for a given problem will depend on the conditioning of V (which in turn is controlled by the distribution of its nodes) as well as the number of right-hand sides, and the size of the problem. A summary for practitioners is as follows:

Which solver should you use? Conclusions based on our experiments.

- For single right-hand side problems that have nearly equispaced or only mildly clustered nodes, use iterative methods applied to the normal equations or adjoint normal equations (see [Figure 5](#) and [Figure 6](#)).
- For small-to-moderate-scale problems with many right-hand sides and only mildly clustered nodes, use the Kircheis–Potts method [34].
- For moderate-to-large-scale problems with multiple right-hand sides, or for any problems with irregular or highly-clustered nodes, use the proposed ADI-based least-squares solver, or a direct Toeplitz solver on the normal equations if conditioning permits (see [Figure 6](#) and [Figure 7](#)).

A couple of caveats: while we include some commentary on preconditioning, we only engage with some of the large literature on preconditioning for Toeplitz systems of linear equations [14]. We also do not include any commentary related to parallelization. We discuss some aspects of noise in the context of signal reconstruction in [subsection 5.3](#), but there remains more to investigate in future work. The MATLAB/Octave codes to reproduce all experiments is found at <https://github.com/heatherw3521/NUFT>.

In most experiments, test signals are created by generating random complex-valued coefficients $(\{x_k\}_{k=1}^n)$ in (1.1) whose real and imaginary parts are independently drawn from the normal distribution of zero mean and unit variance. This is a simple model for complex-valued signals of bandwidth n , and hence (when interpreted as symmetrized frequency indices $-n/2 \leq k < n/2$ as in [Remark 1](#)) bandlimit $n/2$. We have found that scaling with a k -dependent decay does not qualitatively affect the results. In [subsection 5.3](#) only we instead choose coefficients to give a known 1D “image.” We usually choose $\{b_j\}_{j=1}^m$ so that (1.1) is consistent, except in [subsection 5.3](#) where the second test adds noise to the data.

We consider the following four schemes for generating the locations $\{p_j\}_{j=1}^m \subset [0, 1]$, which are designed to lead to increasingly poorly conditioned problems. [Figure 4](#) shows examples of the resulting unit circle nodes $\gamma_j = e^{-2\pi i p_j}$.

Grid 1: We set $p_j = ((m - j + 1) + \theta\psi_j)/m$, where ψ_j is drawn from a uniform distribution on $[-1, 1]$, giving a jittered regular grid with θ the so-called “jitter parameter”. When $0 \leq \theta < 1/4$, V is proven to be well-conditioned in the square case $m = n$ [2, 65]. For our overdetermined experiments with $m/n \approx 2$, we choose $\theta = 1/2$ and observe very good conditioning ($\kappa_2(V) \approx 2.0$, independent of n).

Grid 2: We use Chebyshev points of the second kind for $(0, 1)$, which are given by the formula $p_j = (1 + \cos \frac{\pi(j-1)}{m-1})/2$. These are also Clenshaw–Curtis quadrature nodes. The resulting nodes of V exhibit strong clustering along the circle toward the point $z = 1$, and the first and last nodes coincide. The largest gap $p_{m/2} - p_{m/2+1}$ is

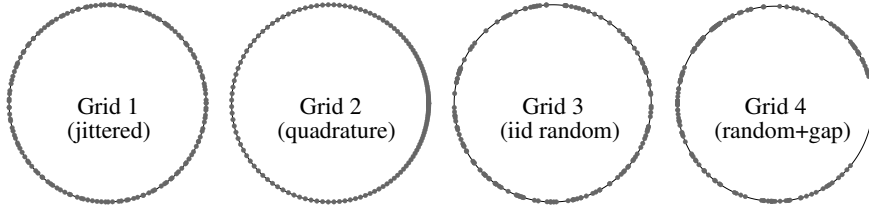


Fig. 4: Node sets $\{\gamma_j\}_{j=1}^m$ from the four kinds of nonuniform distributions tested in [section 5](#). The first two give $\kappa_2(V) = \mathcal{O}(1)$, while for the last two $\kappa_2(V)$ is large ($\gg 10^4$ in large problems). For visibility, a very small mode number $m = 150$ is shown. In Grid 4 the gap is four wavelengths at the Nyquist frequency $n/2$, choosing $n = m/2$.

close to $\pi/2m$. The condition that this gap be narrower than half a wavelength at the Nyquist frequency $n/2$ leads to the condition $m/n > \pi/2$; when this holds we observe $\kappa_2(V)$ small (of order 10, with very weak growth in n). Conversely, for $m/n < \pi/2$ we see exponentially poor conditioning.

- Grid 3: The p_j are independently uniform random on $[0, 1)$, then sorted in descending order. This leads to random gaps, with an expected largest gap of $\mathcal{O}(m^{-1} \log m)$. For $m/n \approx 2$, we observe $\kappa_2(V)$ large and growing with n , of order 10^4 for $n \approx 2000$ (the largest SVD we have computed). The singular value spectrum appears to densely fill the interval $[0, \sigma_{\max}(V)]$ somewhat uniformly.
- Grid 4: The p_j are independently uniform random on $[0, 1 - \delta]$, again sorted, where the enforced gap size is $\delta = 8/n$, corresponding to 4 wavelengths at the Nyquist frequency of $n/2$. The gap results in significantly higher $\kappa_2(V)$ than for Grid 3, namely in the range 10^6 to 10^8 for the largest SVDs we computed. Apart from the few smallest singular values, the overall singular value spectrum is similar to that of Grid 3.

5.1. Iterative methods vs. ADI-based direct solver. We compare timings⁶ and relative residual error across several iterative methods in [Figure 5](#). The algorithms are implemented in MATLAB R2023a, where each iteration uses either MATLAB’s FFT library, or the MATLAB wrapper for the state of the art FINUFFT library [5] for NUDFT transforms (multiplications by V or V^*). We compare against five iterative methods we call CG nor, PCG nor Strang, FP adj sinc, CG adj, and PCG adj sinc; see [Appendix A](#) for a description of these methods.

The performance of these methods is compared to the proposed ADI-based least-squares direct solver in [Figure 5](#), for a large problem of size $524,288 \times 262,144$ (oversampling ratio $m/n = 2$). The iterative methods terminate by either achieving a relative residual of 10^{-7} or performing a maximum number of iterations (8,000 for methods on adjoint equations, 10,000 for methods on normal equations).

The convergence of the iterative methods depends in general on the singular value distribution of V and on the right-hand side [3, 13]; a well-known bound on its geometric rate is controlled by the condition number $\kappa_2(V)$ [52]. The latter diverges as the nodes become increasingly irregular. Grids 1 and 2 do not cause much trouble (iteration counts are in the range 10–100), but all of the iterative methods struggle when Grids 3 and 4 are used. For example, CG on the normal equations requires 5734 and 5416 iterations, respectively, and CG on the adjoint normal equations requires 7788 and 7769 iterations, respectively. The

⁶For experiments in this section, all methods were tested using a Dell laptop computer with a 12th Gen Intel Core i7-1280P 1.8 GHz processor and 32 GB RAM.

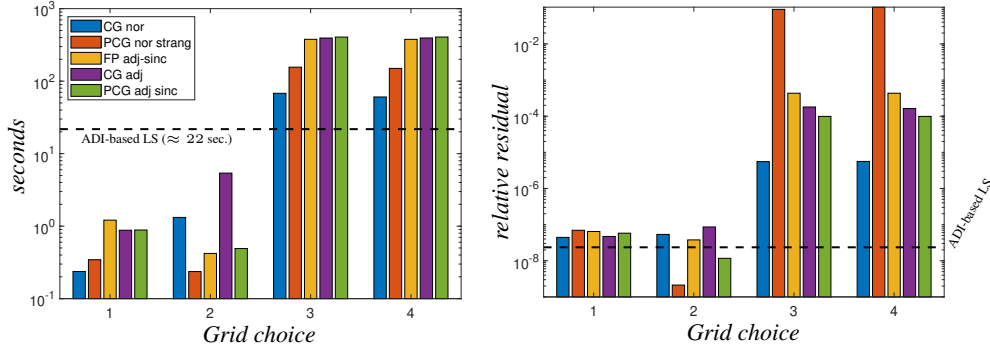


Fig. 5: The bar plots compare the performances of various iterative methods with the proposed ADI-based least-squares solver for solving $Vx = b$ for the four different node sets (grids) of Figure 4. V is of size $m \times n = 524, 288 \times 262, 144$. *Left:* The wall clock time in seconds achieved by each method is plotted on a log scale for each grid choice. The ADI-based LS method (dotted black line) is insensitive to the grid choice and performs similarly (about 22 seconds) for all problems of this size. *Right:* The relative 2-norm residual (data error) achieved by each method is plotted on a log scale for each grid choice. The ADI-based least-squares method achieves roughly the same relative residual for every problem. The HSS rank parameter is $\epsilon = 10^{-10}$. In most of the iterative methods for grids 3 and 4, a maximum iteration count around 10^4 was reached (see subsection 5.1).

two types of preconditioning tested do not seem to help here. In contrast, the ADI-based least-squares solver is agnostic to the grid choice, and always takes around 22 seconds to execute for this problem size. Here, the HSS rank parameter is set as $\epsilon = 10^{-10}$.

An informative comparison of the methods is given in Figure 6, where we plot the relative residual against the execution time per right-hand-side required to achieve it⁷. Unlike the iterative methods, the ADI-based least-squares solver gains efficiency as the number of right-hand sides is increased. For this test, V is of size $29, 492 \times 16, 384$ (so oversampling $m/n \approx 1.8$), with Grid 3 used for sample locations. Various stopping residuals are explored for the iterative methods⁸. One conclusion we draw is that if 20 or more RHS are needed, the ADI-based solver beats all iterative methods, even at low accuracy.

5.2. Comparisons with direct methods. Here, we compare against some alternative direct solvers, including the method from Kircheis and Potts in [34] and an ADI-based Toeplitz solver we have implemented and applied to solve the normal equations. Overall, we find that the specialized ADI-based solvers are much faster and more robust than other direct solvers currently available. For those familiar with hierarchical solvers, it may be surprising that the ADI-based methods perform as well as they do on small- and moderate-sized problems. The computational and memory costs for hierarchical methods often involve large constants, making them useful primarily in the large-scale setting. Our HSS construction method is leaner than many hierarchical solvers because we heavily leverage the displacement structure of V (e.g., to avoid forming or storing V or C outright, to supply explicit a priori bounds for low

⁷We omit CG with Strang preconditioning from these results as it performed much more poorly than other methods.

⁸Interestingly, the residual error for the iterative methods appears to decay only algebraically (rather than geometrically) with iteration count. This type of *sublinear* CG convergence has been observed [13, Fig. 1] and analyzed [3, Sec. 3.2] when the eigenvalue spectrum densely fills an interval that includes zero, which seems to be the case for Grid 3. We leave a full understanding for future work.

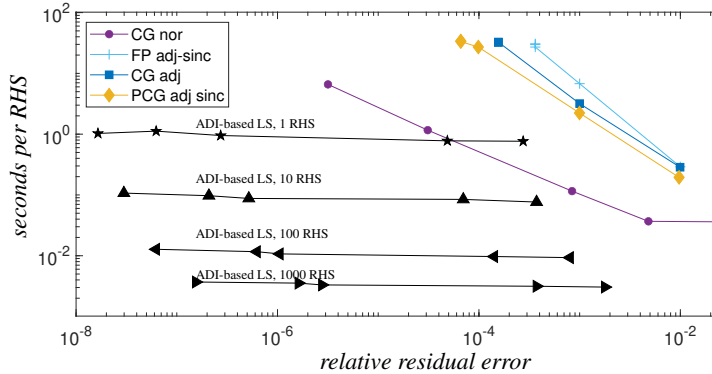


Fig. 6: The performances of several methods are compared by plotting the relative residual error achieved against the execution time required to achieve it on a log-log scale. Execution times indicate the time per right-hand side, which for the iterative methods only depends on accuracy (residual). The proposed ADI-based direct method has a run-time almost independent of accuracy, and shows an efficiency per RHS growing linearly up to several hundred RHS. In these problems, Grid 3 is used to generate the $29,492 \times 16,384$ matrix V .

rank approximations, and to apply an unusually fast low rank approximation method).

In the left panel of Figure 7, we compare the performance of our method against the Kircheis–Potts method [34] for a single right-hand side⁹. The Kircheis–Potts method is designed to be effective in settings where the nodes are not too irregularly clustered and there are many right-hand sides. The method has a $\mathcal{O}(m^2 + n^2)$ precomputation step that can be prohibitive in the large-scale setting. We also compare against dense direct solution (MATLAB’s `mldivide`, i.e., “backslash”), as well as the fast ADI-based Toeplitz solver from [60, Ch. 4] applied to the normal equations (A.1). The latter is the natural Toeplitz analog of our direct least-squares method for Vandermonde matrices. As shown in [60, Ch. 4], the performance of this Toeplitz solver is comparable to related implementations [64] that use randomized numerical linear algebra for HSS construction.

For all of these methods, the cost for solving the system with multiple right-hand sides should be considered in stages. In the first stage, a factorization is computed and stored. For our solvers, this is the hierarchical ULV/URV factorization. For backslash, one could store the factors from QR decomposition. For the Kircheis–Potts method, the initial factorization involves constructing a sparse and diagonal matrix that, along with a DFT matrix, approximately diagonalize the system. The second stage involves applying these factors to the right-hand sides. We supply comparisons for the two fastest methods in Figure 7. Kircheis–Potts requires the application of a sparse matrix-vector product plus an FFT for each right-hand side. Our method also includes an FFT for each right-hand side (step 4 of Algorithm 1.1), plus the hierarchical unitary multiple-triangular solve step in subsection 4.4.2. The solve step applied to multiple right-hand sides involves many dense matrix-matrix products. Since these are handled at the BLAS3 level, we see tremendous practical speedup per right-hand-side at this stage of the computation.

As we see in the left panel of Figure 7, the hierarchical Toeplitz and Vandermonde solvers are the fastest over the other solvers by a factor of 100 when accounting for both stages. For

⁹This test was performed on a 2013 Mac Pro with a 2.7 GHz 12-Core Intel Xeon E5 processor and 64 GB 1866 MHz DDR3 SDRAM

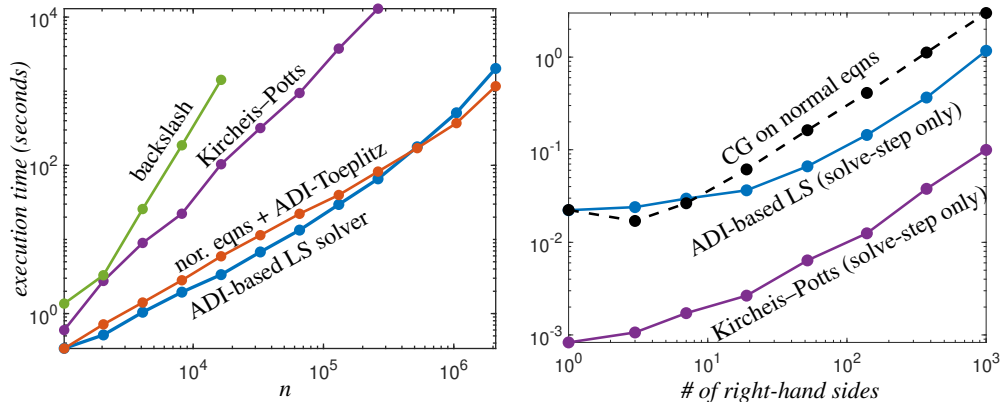


Fig. 7: *Left:* The wall clock time required to solve $Vx = b$, where V is a NUDFT matrix of dimension $2n \times n$ is plotted against n on a log-log scale. We compare the proposed ADI-based LS solver (red) with several other direct methods, including MATLAB’s dense backslash (green), the overdetermined solver from Kircheis and Potts in [34] (purple), and the fast direct ADI-based Toeplitz solver [60, Ch. 4] applied to the normal equations (red). The HSS rank parameter is set to $\epsilon = 10^{-10}$ in the ADI-based solvers. Grid 1 was used, so V is well-conditioned (KP can fail for more ill-conditioned V). *Right:* The execution time in seconds is plotted against the number of right-hand sides in the problem $VX = B$ on a log-log scale for three different solvers, where V is of size 16384×8192 . We exclude factorization steps from the timings. The well-conditioned V is a best-case scenario for CG, which gets slower as V becomes more ill-conditioned. The performance of the ADI-based LS method does not depend on the conditioning of V .

small values of n , our Vandermonde solver outperforms the Toeplitz solver by a small amount, transitioning to slightly underperforming the Toeplitz solver for large values of n . We believe that this performance inversion is due to the Vandermonde solver’s somewhat higher memory requirements. The right panel of Figure 7 shows that the second stage of the Kircheis–Potts solver is about $20\times$ faster than that of the hierarchical Vandermonde solver, showing that the former is very effective for medium-sized problems where the precomputation cost is affordable and the distribution of nodes is not too far from equispaced.

Note that, for this test using Grid 1 (jittered), CG nor was the best iterative method (verified on the left side of Figure 5). Thus we did not include the other four iterative methods in these tests. We also do not include comparisons against $\mathcal{O}(n^2)$ Toeplitz solvers that exploit the Gohberg–Semençul formulae, since in initial tests using the NFFT implementation [33] we found it uncompetitive even at small scale, having a runtime exceeding that of the Kircheis–Potts method [34].

5.3. An “image” reconstruction example. One of the major applications for non-uniform discrete Fourier transforms is signal reconstruction problems. In our previous experiments, we have considered the ideal case where the signal has little structure (all Fourier coefficients with the same variance), while the measurements b_j are free of noise. In practice, measurements are always corrupted with noise, so that $Vx = b$ becomes inconsistent. Yet a true least-squares solution as in (1.1) can effectively average this noise if V is well conditioned. If not, noise will usually be grossly amplified, demanding regularization of the problem (see subsection 6.1).

For now, we make some preliminary observations using a toy 1D reconstruction task. In

Figure 8, we choose a discontinuous signal function $f(2\pi p)$ on $0 \leq p < 1$, where

$$f(x) = \begin{cases} \sin(8x^2), & x < 3 \\ 1, & \frac{7}{2} < x < \frac{9}{2} \\ \max(0, 1 - 2|x - \frac{11}{2}|), & \text{otherwise} \end{cases}$$

contains an oscillatory chirp, a top-hat and a triangle part. Its exact Fourier coefficients

$$c_k = \int_0^1 e^{2\pi i k p} f(2\pi p) dp$$

for $-n/2 \leq k < n/2$ are approximated using equispaced quadrature on $10n$ nodes. We then set $x_k = \exp(-0.5(7k/n)^2)c_k$ which low-pass filters the signal to make it approximately bandlimited (here the Gaussian factor is about 0.002 at the maximum frequency $\pm n/2$). These $\{x_k\}_{-n/2}^{n/2-1}$ are now taken as the true Fourier coefficients. For a given sample grid, $b_j = \sum_{k=-n/2}^{n/2-1} \gamma_j^k x_k$ is evaluated using a type-II. For these experiments, we choose $n = 2048$ and take $m = 3687$ samples of the signal, so $m/n \approx 1.8$. In order to apply NUDFT type-II solvers as defined in the rest of this paper with frequencies $0, \dots, n-1$ offset by $n/2$ from this, prephased data $\gamma_j^{n/2} b_j$ must be used (Remark 1). We solve the least-squares inverse type-II NUDFT problem using two iterative methods (CG on the normal and the adjoint normal equations) and one direct method (ADI-based least-squares solver). This constructs an approximation to the coefficients in (1.1), from which the signal (Fourier series) is plotted on a denser grid of $6n$ equally-spaced points using a padded plain FFT.

We consider two problematic settings. First, we use Grid 4, which results in multiple sizeable gaps between sampling points (one forced, others due to random uniform sampling). This corresponds to large condition number, with $\kappa_2(V) \approx 10^7$. Thus, one would not be able to recover the ground truth in a realistic (noisy) setting. However, with noise-free data we see that the reconstruction via the ADI-based direct solver is visually indistinguishable from the true signal, while the two iterative solvers have $\mathcal{O}(1)$ errors at certain problematic locations (large gaps). This reflects the smaller residual error that the direct solver achieves. The upper right panel of Figure 8 is a zoomed-in display of a small portion of these reconstructions that clearly illustrates these behaviors. While we do not display results for other direct solvers (e.g., the Toeplitz direct solver on the normal equations and backslash in MATLAB), we observe that reconstructions from these methods look similar to the ADI-based result. This illustrates an accuracy advantage that fast direct solvers can have in ill-conditioned settings.

In the lower left panel of Figure 8, we consider another problematic setting. Here, we sample the signal using Grid 1 (jittered), so that V is well-conditioned, but then add iid Gaussian noise of standard deviation 10^{-2} to both the real and complex parts of the observations (visible as blue dots in lower-right panel), to give the right-hand side vector in $Vx = b$. The oversampling helps average away (reduce) some noise in the solutions from CG on the normal equations and the ADI-based direct solver. Moreover these two solutions are extremely close, differing by about 10^{-5} in the L^2 -norm. In contrast, the CG on adjoint normal equations is visibly much noisier.

6. Extensions. Various extensions and future investigations arise from this work. Some extensions are immediate, while some are more involved.

6.1. Regularization. Regularization is essential to retain some degree of stability of the solution for ill-conditioned Fourier inverse problems, and in the noisy data case may be interpreted as a prior on x [11, 46, 59]. A general Tikhonov-regularized type-II inverse

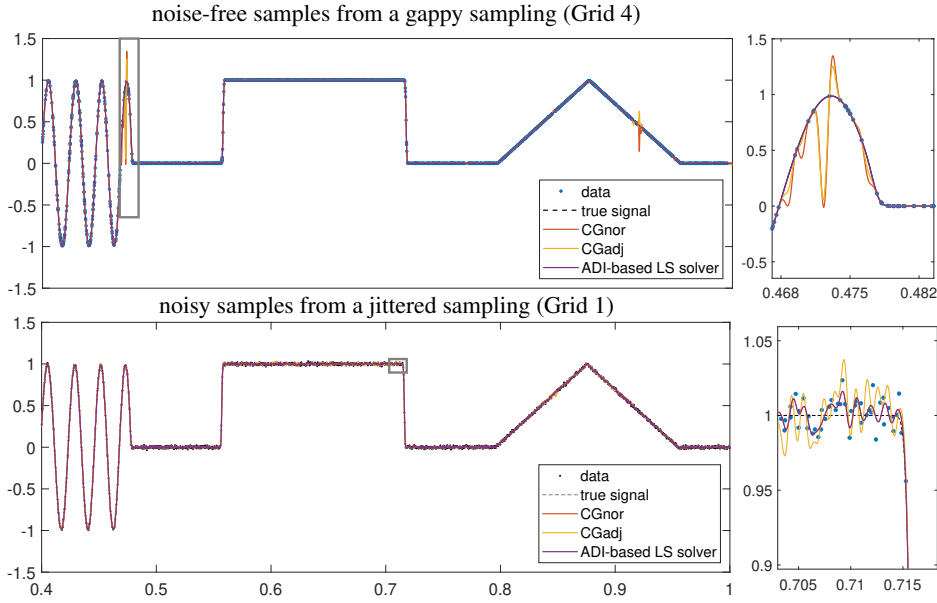


Fig. 8: 1D “image” reconstruction example with $n = 2048$ coefficients and $m = 3687$. Samples are shown only on a subset of the domain where $0.4 < p_m < 1$. *Upper*: The real part of several reconstructions of a signal are plotted on a fine regular grid, along with the true underlying signal (obscured as it closely coincides with the ADI-based reconstruction). The blue dots indicate samples. The sample locations are given by Grid 4 (iid random with gap). The grey rectangle highlights a portion of the signal that is zoomed in on to the right. *Lower*: Reconstructions for the same signal but using Grid 1 (jittered), with data corrupted by additive noise. The grey rectangle highlights a portion of the signal zoomed in on to the right, where one sees that the CG nor and ADI-based reconstructions visually coincide.

NUDFT problem takes the form

$$x = \operatorname{argmin}_{x \in \mathbb{C}^n} \|Vx - b\|_2^2 + \lambda x^* Lx, \quad (6.1)$$

where $\lambda > 0$ is a regularization parameter and L is a symmetric positive semidefinite matrix. The normal equations for this problem are $(V^*V + \lambda L)x = V^*b$. Forming and solving the normal equations can be numerically problematic if V is ill-conditioned. Instead, we can pursue an alternate approach using the *expanded equations*

$$\begin{bmatrix} -\alpha I & V \\ V^* & (\lambda/\alpha)L \end{bmatrix} \begin{bmatrix} r \\ x \end{bmatrix} = \begin{bmatrix} b \\ 0 \end{bmatrix}. \quad (6.2)$$

The parameter $\alpha > 0$ can be tuned to improve the condition number of the matrix on the right-hand side.¹⁰ The x part of the solution to the expanded equations is the solution to the regularized least-squares problem (6.1).

Using the transformed matrix $C = VF^*$, the expanded equations (6.2) can be reformu-

¹⁰For the un-regularized case $\lambda = 0$, the choice $\alpha = \sigma_{\min}(V)/\sqrt{2}$, the augmented matrix on the left-hand side of (6.2) is guaranteed to have a condition number less than $2\kappa_2(V)$ [12, eq. (2.6)]. It is less clear how to choose this parameter for $\lambda \neq 0$.

lated as

$$\begin{bmatrix} -\alpha I & C \\ C^* & (\lambda/\alpha)(FLF^*) \end{bmatrix} \begin{bmatrix} r \\ \tilde{x} \end{bmatrix} = \begin{bmatrix} b \\ 0 \end{bmatrix}. \quad (6.3)$$

This is a square linear systems of equations with HSS off-diagonal blocks. Whether (6.3) can be efficiently solved depends on the matrix L . For the simple case $L = I$, the matrix in (6.3) will be an HSS matrix with HSS rank $2k$ after conjugation by a block perfect shuffle permutation. The HSS generators of this permuted matrix can be obtained from the HSS generators of C . Thus, for $L = I$, (6.3) can be solved in $\mathcal{O}((m/n)^2 \cdot mk^2)$ operations by a ULV HSS solver [15].¹¹ The question of whether (6.3) can be solved efficiently for other L matrices is a topic for future work.

6.2. The type-I NUFT. The inverse type-I NUFT problem is the transpose of the problem considered in this paper. Consider known Fourier series coefficients b_k , say labeled $k = 1, \dots, m$, and source locations $p_j \in [0, 1)$, $j = 1, \dots, n$, then one solves for the strengths x_j of these sources that generates the known coefficients. I.e., one solves $\tilde{V}x = b$ where $\tilde{V}_{kj} = \gamma_j^{k-1}$ defines an $m \times n$ transposed Vandermonde matrix. Note that the roles of m and n are swapped relative to the type-II. This problem has applications to superresolution (finding strengths x of closely-spaced sources given far-field data b). Because the unknowns are now at nonuniform locations, the character is quite different (see Remark 2). The matrix $\tilde{F}\tilde{V}$ is Cauchy-like, and one can apply similar ADI-based strategies to approximate it with an HSS matrix. In the overdetermined case $m \geq n$, the solver in subsection 4.2 can be applied directly. Otherwise for $m < n$ the solution to the inverse NUFT problem is non-unique, and one can either take the solution of minimum norm, or regularize the problem, to insure uniqueness. A semidirect method for the underdetermined case can be found in [29].

6.3. Other matrices with fast diagonalizable displacement structures. This same technique can be applied to solve $Xy = f$ for any matrix X that satisfies a Sylvester matrix equation $AX - XB = F$ where (i) the rank of F is small (e.g., 1 or 2), and (ii) the matrices A and B can be diagonalized via fast transforms. This includes Toeplitz, Hankel, and Toeplitz+Hankel matrices, as well as nonuniformly sampled Chebyshev-Vandermonde matrices [36].

6.4. The 2D NUFT. The type-II 2D NUFT considers a list of N ordered pairs of sample locations, $\{(t_1, s_1), \dots, (t_m, s_m)\} \subset [0, 1]^2$, with corresponding samples $\{b_1, \dots, b_m\}$. For type-II 2D NUFT, the goal is to recover the coefficient matrix X in

$$b_j = \sum_{k=1}^{n_1} \sum_{k'=1}^{n_2} e^{-2\pi i((k-1)t_j + (k'-1)s_j)} X_{kk'}, \quad 1 \leq j \leq m. \quad (6.4)$$

If the sample locations $\{(t_j, s_j)\}$ form a tensor grid on $[0, 1]^2$, then a fast 2D solver follows directly from repeated applications of the 1D solvers. However, one should not expect this to be the case for an arbitrary problem. In general, we can express (6.4) as an $m \times n_1 n_2$ linear system involving a multivariate Vandermonde matrix V . One can also view V as the face-splitting product [54] $V_\eta \bullet V_\xi$, where V_η is the $m \times n_1$ Vandermonde matrix with nodes η , and V_ξ is the $m \times n_2$ Vandermonde matrix with nodes ξ . There are various ways that one can transform V into a matrix involving Cauchy-like structures, but there is no obvious way

¹¹Incidentally, the $\lambda = 0$ case of this approach gives an alternate fast direct solver for the un-regularized type-II NUFT inverse problem (1.2). This approach pays a quadratic penalty in the ‘‘rectangularity’’ m/n over the rectangular HSS-based approach developed in this paper, but it can be useful in a pinch if one only has access to a square HSS solver.

to transform V into a matrix that is well-approximated by an HSS matrix. Explaining and exploiting the structures and low rank properties of V (or possibly V^*V) is an area of ongoing investigation. A closely related investigation involves the formulation of preconditioners based on the structures of V .

Acknowledgments. The authors are grateful for discussions with Dima Batenkov, Leslie Greengard, Alex Townsend, and Joel Tropp, as well as support to attend a workshop at Casa Matemática Oaxaca (Banff International Research Station) where some early work was done. This work is partly supported by the National Science Foundation under grant DMS-2103317 and FRG award 1952777, the Carver Mead New Horizons Fund, and the U.S. Department of Energy, Office of Science, Office of Advanced Scientific Computing Research, Department of Energy Computational Science Graduate Fellowship under award number DE-SC0021110¹². We thank Joel Tropp for access to the machine used to make the left panel of [Figure 7](#). The Flatiron Institute is a division of the Simons Foundation.

Appendix A. Description of iterative methods. Here is a description of the iterative methods with which we compare in [subsection 5.1](#):

1. **CG nor.** The conjugate gradient method is applied to the normal equations

$$V^*Vx = V^*b, \quad (\text{A.1})$$

where the Toeplitz matrix with entries $(V^*V)_{kk'} = \sum_{j=1}^m \gamma_j^{k'-k}$ is applied via discrete nonperiodic convolution using the padded¹³ FFT. Here, the Toeplitz vector is precomputed by applying the type-I NUDFT to the vector of ones. CG on the normal equations minimizes the residual 2-norm as in (1.2), and is thus also known as CGNR [52, §8.3].

2. **PCG nor Strang.** We apply Strang preconditioning [14, §2.1] to the previous CG method for (A.1): this uses a $n \times n$ circulant preconditioner constructed from the central n diagonals of the Toeplitz matrix. Such a preconditioner is generally effective for diagonally-dominant matrices, which does not generally hold for V^*V .
3. **FP adj sinc.** We include a fixed-point iteration found to be effective in the MRI setting by Inati et al. [30] to solve the adjoint (“second kind”) $m \times m$ normal equations

$$VV^*z = b, \quad (\text{A.2})$$

returning $x = V^*z$. Assuming that W is an approximate inverse of VV^* , then from the current guess z_k the residual $r_k = VV^*z_k - b$ is computed, from which the next iterate is $z_{k+1} = z_k - Wr_k$. This iteration starts with $z_0 = b$, and stops when $\|r_k\| \leq \epsilon\|b\|$. Turning to W , a good diagonal choice is given by the Frobenius norm minimization

$$w = \underset{w \in \mathbb{R}^m, W = \text{diag}\{w\}}{\text{argmin}} \|I - WV^*V\|_{\mathbb{F}}^2, \quad (\text{A.3})$$

motivated by the fact that the convergence rate of the above iteration is bounded by the spectral norm $\|I - WV^*V\|$, yet the Frobenius norm is much simpler to

¹²**Disclaimer:** This report was prepared as an account of work sponsored by an agency of the United States Government. Neither the United States Government nor any agency thereof, nor any of their employees, makes any warranty, express or implied, or assumes any legal liability or responsibility for the accuracy, completeness, or usefulness of any information, apparatus, product, or process disclosed, or represents that its use would not infringe privately owned rights. Reference herein to any specific commercial product, process, or service by trade name, trademark, manufacturer, or otherwise does not necessarily constitute or imply its endorsement, recommendation, or favoring by the United States Government or any agency thereof. The views and opinions of authors expressed herein do not necessarily state or reflect those of the United States Government or any agency thereof.

¹³We pad to $2n$ since it is much more efficient for FFTs than the minimum padding length of $2n - 1$.

minimize than the spectral norm. Specifically, the exact solution to (A.3) may easily be found to be the have elements

$$w_j = \frac{(VV^*)_{jj}}{(VV^*VV^*)_{jj}} = \frac{n}{\sum_{j'=1}^m |(VV^*)_{jj'}|^2}, \quad j = 1, \dots, m, \quad (\text{A.4})$$

which may be interpreted as the discrete analog of “sinc² weights” in the MRI literature [18, 27], since the Dirichlet kernel entries obey

$$\lim_{n \rightarrow \infty} (VV^*)_{jj'} = n \operatorname{sinc} n\pi(p_j - p_{j'});$$

also see [35, Rmk. 3.16]. An efficient computation of w groups terms along each diagonal $q = k - k'$ as follows:

$$(VV^*VV^*)_{jj} = \sum_{k, k'=1}^n \gamma_j^{k-k'} \sum_{j'=1}^m \gamma_{j'}^{k'-k} = \sum_{|q| < n} \gamma_j^q \cdot (n - |q|) \sum_{j'=1}^m \overline{\gamma_{j'}^{-q}},$$

which can now be evaluated by a type-I NUDFT with unit strengths, followed by a type-II (each transform being double-sized with shifted frequency range). The triangular weights $(n - |q|)$ show that the denominator in (A.4) is a *Fejér kernel*.

4. **CG adj.** This applies CG to (A.2), where the matrix VV^* is, as above, applied by a type-I and then type-II transform. $x = V^*z$ is then returned. In this case CG minimizes the 2-norm of the error in x , as opposed to the residual, and is also known as CGNE or Craig’s method [52, §8.3].
5. **PCG adj sinc.** This uses the diagonal matrix $W = \operatorname{diag}\{w\}$ with the optimal (“sinc²” or Fejér) weights (A.4) as the preconditioner for CG on (A.2), as a variant of the previous method. This is discussed in [27, Rmk. 1].

REFERENCES

- [1] B. ADCOCK, M. GATARIC, AND A. HANSEN, *On stable reconstructions from nonuniform Fourier measurements*, SIAM J. Imaging Sci., 7 (2014), pp. 1690–1723.
- [2] A. P. AUSTIN AND L. N. TREFETHEN, *Trigonometric interpolation and quadrature in perturbed points*, SIAM J. Numer. Anal., 55 (2017), pp. 2113–2122.
- [3] O. AXELSSON AND I. KAPORIN, *On the sublinear and superlinear rate of convergence of conjugate gradient methods*, Numer. Algor., 25 (2000), pp. 1–22.
- [4] S. BAGCHI AND S. MITRA, *The nonuniform discrete Fourier transform*, in Nonuniform Sampling: Theory and Practice, Springer, 2001, pp. 325–360.
- [5] A. H. BARNETT, J. MAGLAND, AND L. AF KLINTEBERG, *A parallel nonuniform fast Fourier transform library based on an “exponential of semicircle” kernel*, SIAM J. Sci. Comput., 41 (2019), pp. C479–C504.
- [6] D. BATENKOV, B. DIEDERICHS, G. GOLDMAN, AND Y. YOMDIN, *The spectral properties of Vandermonde matrices with clustered nodes*, Lin. Alg. Appl., 609 (2021), pp. 37–72.
- [7] F. S. BAZÁN, *Conditioning of rectangular Vandermonde matrices with nodes in the unit disk*, SIAM J. Matrix Anal. Appl., 21 (2000), pp. 679–693.
- [8] M. BEBENDORF, *Hierarchical matrices*, Springer, 2008.
- [9] B. BECKERMANN AND A. TOWNSEND, *On the singular values of matrices with displacement structure*, SIAM J. Matrix Anal. Appl., 38 (2017), pp. 1227–1248.
- [10] P. BENNER, R.-C. LI, AND N. TRUHAR, *On the ADI method for Sylvester equations*, J. Comput. Appl. Math., 233 (2009), pp. 1035–1045.
- [11] M. BERTERO AND P. BOCCACCI, *Introduction to inverse problems in imaging*, Institute of Physics Publishing, Ltd, 1998.
- [12] Å. BJÖRCK, *Iterative refinement of linear least squares solutions I*, BIT, 7 (1967), pp. 257–278.
- [13] E. CARSON, J. LIESEN, AND Z. STRAKOŠ, *Towards understanding CG and GMRES through examples*, Linear Algebra Appl., 692 (2024), pp. 241–291.

- [14] R. H.-F. CHAN AND X.-Q. JIN, *An introduction to iterative Toeplitz solvers*, SIAM, 2007.
- [15] S. CHANDRASEKARAN, M. GU, AND T. PALS, *A fast ULV decomposition solver for hierarchically semiseparable representations*, SIAM J. Matrix Anal. Appl., 28 (2006), pp. 603–622.
- [16] S. CHANDRASEKARAN, M. GU, X. SUN, J. XIA, AND J. ZHU, *A superfast algorithm for Toeplitz systems of linear equations*, SIAM J. Matrix Anal. Appl., 29 (2007), pp. 1247–1266.
- [17] H. CHENG, Z. GIMBUTAS, P.-G. MARTINSSON, AND V. ROKHLIN, *On the compression of low rank matrices*, SIAM J. Sci. Comput., 26 (2005), pp. 1389–1404.
- [18] H. CHOI AND D. C. MUNSON, *Analysis and design of minimax-optimal interpolators*, IEEE Trans. Signal Processing, 46 (1998), pp. 1571–1579.
- [19] D. DONOHO AND P. STARK, *Uncertainty principles and signal recovery*, SIAM J. Appl. Math., 49 (1989), pp. 906–930.
- [20] A. DUTT AND V. ROKHLIN, *Fast Fourier transforms for nonequispaced data*, SIAM J. Sci. Comput., 14 (1993), pp. 1368–1393.
- [21] ———, *Fast Fourier transforms for nonequispaced data, II*, Appl. Comput. Harm. Anal., 2 (1995), pp. 85–100.
- [22] H. G. FEICHTINGER, K. GRÖCHENIG, AND T. STROHMER, *Efficient numerical methods in non-uniform sampling theory*, Numer. Math., 69 (1995), pp. 423–440.
- [23] J. A. FESSLER, S. LEE, V. T. OLAFSSON, H. R. SHI, AND D. C. NOLL, *Toeplitz-based iterative image reconstruction for MRI with correction for magnetic field inhomogeneity*, IEEE Trans. on Sig. Proc., 53 (2005), pp. 3393–3402.
- [24] I. GOHBERG, T. KAILATH, AND V. OLSHEVSKY, *Fast Gaussian elimination with partial pivoting for matrices with displacement structure*, Math. of Comp., 64 (1995), pp. 1557–1576.
- [25] D. GREEN, J. JAMORA, AND A. GELB, *Leveraging joint sparsity in 3D synthetic aperture radar imaging*, Appl. Math. Modern Chall., 1 (2023), pp. 61–86.
- [26] L. GREENGARD AND J.-Y. LEE, *Accelerating the nonuniform fast Fourier transform*, SIAM Rev., 46 (2004), pp. 443–454.
- [27] L. GREENGARD, J.-Y. LEE, AND S. INATI, *The fast sinc transform and image reconstruction from nonuniform samples in k -space*, Comm. in Appl. Math. and Comp. Science, 1 (2006), pp. 121–131.
- [28] W. HACKBUSCH, *Hierarchical matrices: algorithms and analysis*, vol. 49, Springer, 2015.
- [29] K. L. HO AND L. GREENGARD, *A fast semidirect least squares algorithm for hierarchically block separable matrices*, SIAM J. Matrix Anal. Appl., 35 (2014), pp. 725–748.
- [30] S. INATI, J.-Y. LEE, L. FLEYSHER, R. FLEYSHER, AND L. GREENGARD, *Iterative reconstruction of magnetic resonance images from non-uniform samples in k -space*, 2006. unpublished manuscript.
- [31] M.-P. ISTACE AND J.-P. THIRAN, *On the third and fourth Zolotarev problems in the complex plane*, SIAM J. Numer. Anal., 32 (1995), pp. 249–259.
- [32] T. KAILATH AND A. H. SAYED, *Displacement structure: theory and applications*, SIAM Rev., 37 (1995), pp. 297–386.
- [33] J. KEINER, S. KUNIS, AND D. POTTS, *Using NFFT3—a software library for various nonequispaced fast Fourier transforms*, ACM Transactions on Mathematical Software (TOMS), 36 (2009), pp. 1–30.
- [34] M. KIRCHEIS AND D. POTTS, *Direct inversion of the nonequispaced fast Fourier transform*, Lin. Alg. Appl., 575 (2019), pp. 106–140.
- [35] M. KIRCHEIS AND D. POTTS, *Fast and direct inversion methods for the multivariate nonequispaced fast Fourier transform*, Front. Appl. Math. Stat., (2023).
- [36] P. KOEV, *Matrices with displacement structure—a survey*. <https://math.mit.edu/~plamen/files/mds.pdf>, 1999.
- [37] S. KUNIS AND D. NAGEL, *On the condition number of Vandermonde matrices with pairs of nearly-colliding nodes*, Numer. Algor., 87 (2021), pp. 473–496.
- [38] S. KUNIS AND D. POTTS, *Stability results for scattered data interpolation by trigonometric polynomials*, SIAM Journal on Scientific Computing, 29 (2007), pp. 1403–1419.
- [39] ———, *Time and memory requirements of the nonequispaced FFT*, Sampling Theory in Signal and Image Processing, 7 (2008), pp. 77–100.
- [40] V. LEBEDEV, *On a Zolotarev problem in the method of alternating directions*, USSR Comput. Math. Math. Phys., 17 (1977), pp. 58–76.
- [41] J.-R. LI AND J. WHITE, *Low rank solution of Lyapunov equations*, SIAM J. Matrix Anal. Appl., 24 (2002), pp. 260–280.
- [42] F. MARTIN AND E. WEGERT, *Computing the Hilbert transform using biorthogonal spline wavelets*, J. Math. Sci., 189 (2013), pp. 150–163.
- [43] P.-G. MARTINSSON, *A fast randomized algorithm for computing a hierarchically semiseparable representation of a matrix*, SIAM J. Matrix Anal. Appl., 32 (2011), pp. 1251–1274.
- [44] ———, *Fast direct solvers for elliptic PDEs*, SIAM, 2019.
- [45] S. MASSEI, L. ROBOL, AND D. KRESSNER, *hm-toolbox: Matlab software for HODLR and HSS matrices*, SIAM J. Sci. Comput., 42 (2020), pp. C43–C68.
- [46] F. NATTERER AND F. WÜBBELING, *Mathematical Methods in Image Reconstruction*, Mathematical Model-

- ing and Computation, SIAM, Philadelphia, PA, 2001.
- [47] V. PAN, *Structured matrices and polynomials: unified superfast algorithms*, Springer Science & Business Media, 2001.
 - [48] D. W. PEACEMAN AND H. H. RACHFORD, JR., *The numerical solution of parabolic and elliptic differential equations*, J. Soc. for ind. Appl. Math., 3 (1955), pp. 28–41.
 - [49] D. POTTS AND G. STEIDL, *Fast summation at nonequispaced knots by NFFT*, SIAM J. Sci. Comput., 24 (2003), pp. 2013–2037.
 - [50] F.-H. ROUET, X. S. LI, P. GHYSELS, AND A. NAPOV, *A distributed-memory package for dense hierarchically semi-separable matrix computations using randomization*, ACM Transactions on Mathematical Software (TOMS), 42 (2016), pp. 1–35.
 - [51] D. RUIZ-ANTOLIN AND A. TOWNSEND, *A nonuniform fast Fourier transform based on low rank approximation*, SIAM J. Sci. Comput., 40 (2018), pp. A529–A547.
 - [52] Y. SAAD, *Iterative methods for sparse linear systems*, SIAM, Philadelphia, PA, 2nd ed., 2003.
 - [53] M. D. SACCHI AND T. J. ULRYCH, *Estimation of the discrete Fourier transform, a linear inversion approach*, Geophysics, 61 (1996), pp. 1128–1136.
 - [54] V. SLYUSAR, *A family of face products of matrices and its properties*, Cybernetics and Systems Analysis, 35 (1999), pp. 379–384.
 - [55] P. R. SWAN, *Discrete Fourier transforms of nonuniformly spaced data*, Ast. J., 87 (1982), p. 1608.
 - [56] THE MATHWORKS, INC., *nufft: nonuniform fast Fourier transform function, MATLAB version R2024a*. <https://www.mathworks.com/help/matlab/ref/double.nufft.html>.
 - [57] A. TOWNSEND AND H. WILBER, *On the singular values of matrices with high displacement rank*, Lin. Alg. Appl., 548 (2018), pp. 19–41.
 - [58] L. N. TREFETHEN AND D. BAU III, *Numerical Linear Algebra*, SIAM, 1997.
 - [59] A. VISWANATHAN, A. GELB, D. COCHRAN, AND R. RENAUT, *On reconstruction from non-uniform spectral data*, J. Sci. Comput., 45 (2010), pp. 487–513.
 - [60] H. D. WILBER, *Computing Numerically with Rational Functions*, PhD thesis, Cornell University, 2021.
 - [61] Y. XI AND Y. SAAD, *Computing partial spectra with least-squares rational filters*, SIAM J. Sci. Comput., 38 (2016), pp. A3020–A3045.
 - [62] Y. XI, J. XIA, S. CAULEY, AND V. BALAKRISHNAN, *Superfast and stable structured solvers for Toeplitz least squares via randomized sampling*, SIAM J. Matrix Anal. Appl., 35 (2014), pp. 44–72.
 - [63] J. XIA, *A hierarchically semiseparable (HSS) package*. <https://www.math.purdue.edu/~xiaj/packages.html>, 2010. Last edited 2019.
 - [64] J. XIA, Y. XI, AND M. GU, *A superfast structured solver for Toeplitz linear systems via randomized sampling*, SIAM J. Matrix Anal. Appl., 33 (2012), pp. 837–858.
 - [65] A. YU AND A. TOWNSEND, *On the stability of unevenly spaced samples for interpolation and quadrature*, BIT Numerical Mathematics, 63 (2023), p. 23.
 - [66] E. ZOLOTAREV, *Application of elliptic functions to questions of functions deviating least and most from zero*, Zap. Imp. Akad. Nauk. St. Petersburg, 30 (1877), pp. 1–59.
 - [67] P. ZWARTJES AND M. SACCHI, *Fourier reconstruction of nonuniformly sampled, aliased seismic data*, Geophysics, 72 (2007), pp. V21–V32.